Utrecht University

Master Thesis

On the modeling of the initial formation of offshore tidally generated sand waves

Author:
Abel Maarten Scherf

Supervisors:
Prof. Dr. Huib de Swart
Dr. Abdel Nnafie
Co-Supervisor:
MSc. Janneke Krabbendam

A thesis submitted to Utrecht University in partial fulfillment of the requirement for the degree of Master of Science

in the

Institute for Marine and Atmospheric Research
Department of Physics
Faculty of Science

January 5, 2021

Abstract

Sand waves are rhythmic morphological features on the sea bed that are observed in sandy shallow seas. These bed formations occur in large parts of the North Sea and have a typical wavelength of hundred meters and heights of up to 10 meters. Sand waves are dynamic, meaning that they can migrate up to 10 meters per year. Because of their widespread occurrence and the dynamic behavior they may endanger human activities. For example, a migrating sand wave may expose cables from a wind farm or even narrow down ship routes. So, understanding of sand wave behavior is key to safe offshore activities. Characteristics of sand waves, like migration speed and growth, are difficult to monitor for large parts of the sea and are often investigated through (non-)linear stability models. In this study, the sensitivity of sand wave characteristics to environmental parameters, such as water depth, grain size, and tidal current strength, are investigated by applying a linear stability analyses in a process-based model. This model uses a new formulation for the turbulence closure relation and uses site specific environmental parameter input. The model results are compared both with a state of the art numerical model, namely Delft3D, and observations.

Acknowledgements

Firstly, I would like to acknowledge my roommates, who in 2020, became my colleagues and even better friends. Also, I would like to thank my parents for providing me a second home when the walls were closing in on me.

I would also like to acknowledge MSc. Janneke Krabbendam. Janneke, thank you for being so approachable and the endless chats on Teams about sand waves, Delft-3D and what not. Lastly, I would like to thank my supervisors, Prof. Huib de Swart and Dr. Abdel Nnafie. Huib, thank you for giving me the opportunity to grow tremendously in my professional career the past year. You were able to bring across your passion for sediment even when social distancing, which kept me motivated. Abdel, thank you for your words of encouragement and for the cups of espresso (when we were able to work at the IMAU), you really made me feel like a member of the coastal dynamics group.

Contents

1 Introduction

This work will focus on the initial formation of offshore tidal sand waves, which are bottom patterns observed in offshore coastal waters with depths of 10-50 m. Offshore tidal sand waves are formed by the interaction of tidal currents amplitudes of > 0.5 m/s with a sandy bed. This chapter consists of some general information about coastal seas, bottom patterns and sand waves (Section 1.1) followed by some knowledge background of sand waves (Section 1.2), models (Section 1.3), knowledge gaps (Section 1.4), which leads to specific research aims (Section 1.5). Finally, an outline of the thesis is presented (Section 1.6).

1.1 General

Coastal seas are observed all over the world and are located in between the shoreline and the shelf break, where the latter marks the transition to the deep sea. A schematic view of a prototype coastal sea, also called shelf sea, is shown in Figure 1.1. These coastal seas are characterized by shallow water of typically tens to hundred meters deep which can interact freely with the deep ocean where the water depths are typically kilometers. Many of these shelf seas have a sandy bed and water motion that excites sufficiently strong stresses at the bottom to erode and transport sediments. This water motion comprises waves, tides, wind and density-driven currents. Due to nonuniformities in the water motion there will be spatial variations in sediment transport, leading to the formation patterns on the sea bed, which are called bedforms (Dronkers, 2005).

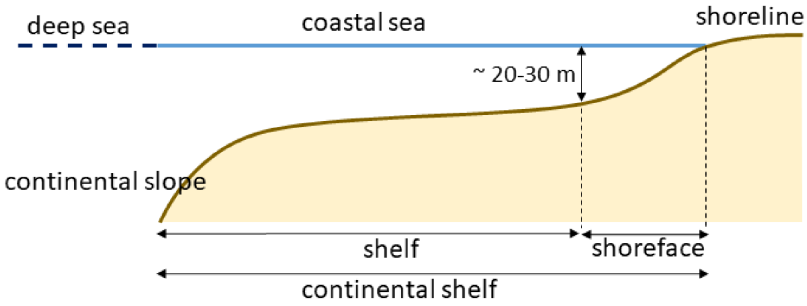

Figure 1.1: Schematic view of a prototype coastal sea, which is located between the shoreline and the continental slope (Krabbendam, 2018).

Coastal bedforms

The spatial scale of coastal bedforms varies widely ranging from several centimeters (ripples) on and near the shoreline, up to several kilometers at the bottom of the shelf sea (tidal sand banks). Table 1 gives an overview of bedforms found on shelf seas including characteristic wavelengths, heights, migration speeds and the time scales on which the bedforms evolve. An example of a shelf sea and the distribution of the bedforms is given in Figure 1.2. In the figure the distribution of bedforms on the North Sea is shown.

Table 1: Overview of bedforms in coastal seas including characteristic wave lengths, height, migration speed and evolution time scale. After Dodd et al. (2003), Knaapen (2005) and Passchier and Kleinhans (2005).

Bedform	Spatial scale [m]	Height [m]	Migration [m/yr]	Time-scale
Ripples	0.1-1	0.01-0.1	1000	Hours
Megaripples	1-15	0.1 - 1.5	100	Days
Sand waves	100-800	1-5	1-10	Decades
Shoreface-connected sand ridges	5000-8000	1-5	1-10	Centuries
Tidal sand banks	5000-10000	5-15	-	Centuries

Probably the most commonly known nearshore bedforms are ripples, which become visible on the beach during low tide. Ripples are not only present on the shoreline, they are also observed submerged further offshore (Soulsby, 1998). Ripples arise from the interaction between the waviness of the bottom and the presence of oscillating currents due to waves in the surf zone. The wavelength, defined as the distance between two successive crests, of the ripples is comparable to the amplitude of the water oscillation at the bed ranging from 10 cm to 1 m, where the crests of the ripples are orthogonal to the direction of wave oscillation (see the review by Blondeaux (2001)). In contrast, megaripples are always submerged in water and can be observed superimposed on larger bedforms in deeper water. They have a characteristic length scale of several meters and attain amplitudes up to 1.5 m (Van Rijn, 1993).
Moving from the shoreline further offshore towards the continental slope, the observed bedforms are sand ridges. These sand ridges have a typical spatial scale in order of several kilometers. The orientation of the seawards end of the ridges are shifted upstream with respect to their shoreface attachments. This shift attains an angle of $20° - 40°$ with the shoreline (Swift et al., 1978). The observed sand ridges in the North Sea are shown in Figure 1.2.
The largest bedforms often can be found the furthest away from the shoreline and are called tidal sand banks (Figure 1.2). They are static with a wavelength of several kilometers, see 1. Huthnance (1982) showed that these tidal sand banks can be explained as a positive feedback between tidal currents and the sandy bottom, i.e. small ridges cause changes in the tidal motion such that, averaged over a tidal period, sediment accumulates at the crests. Here, horizontal residual circulations, generated by tide-topography feedbacks, plays an important role (Zimmerman, 1981).
Other bedforms that are observed on sandy outer continental shelves with tidal current amplitudes of more than 0.5 m/s are tidal sand waves. As these bedforms are the focus of this thesis, they are discussed in a separate subsection.

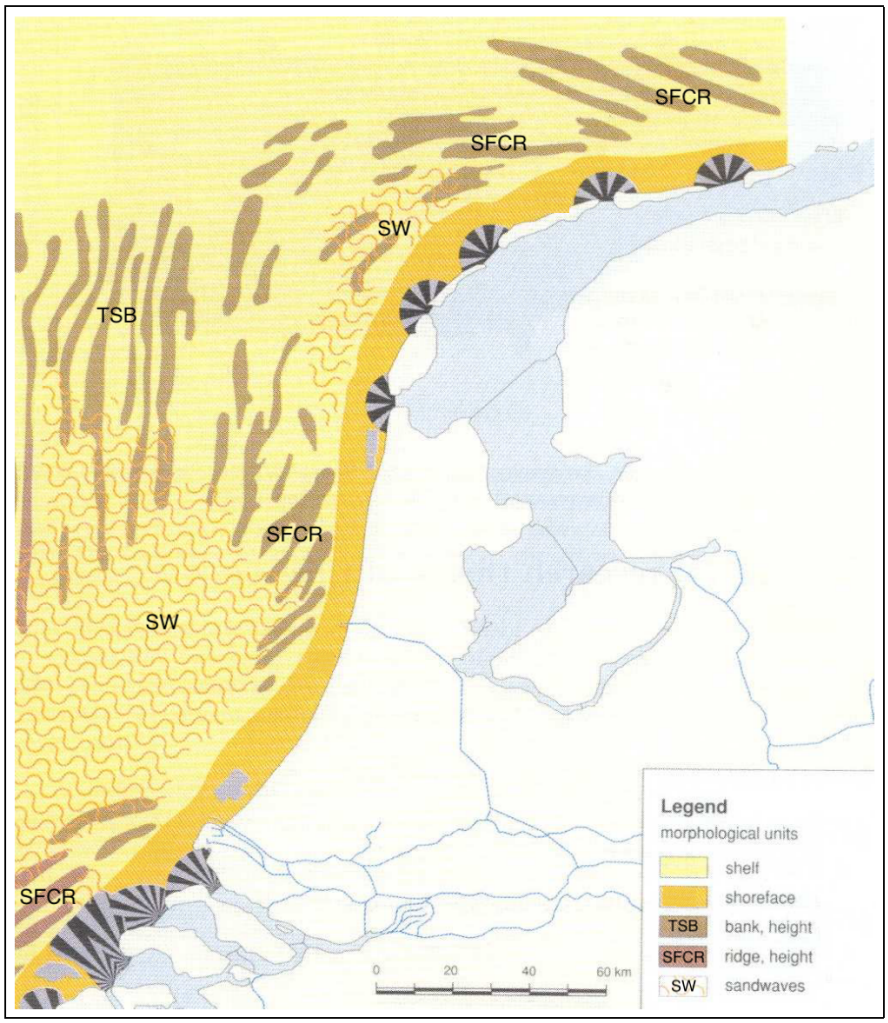

Figure 1.2: Location of sand wave (SW), sand banks (TSB) and shoreface-connected sand ridges (SFCR) in the Dutch coastal waters Van Alphen and Damoiseaux (1989).

1.2 Offshore tidal sand waves

Sand waves are a typical phenomenon of shallow seas, Figure 1.2 indicates the widespread occurrence of offshore tidal sand waves in the North Sea. An example of offshore tidal sand waves, which are also called sand waves, and the seabed profile along a transect is shown in Figure 1.3. Sand waves have a typical wavelength ranging from 100 m to 800 m and can attain a crest-to-trough height difference of meters (Table 1). Their crests are almost orthogonal to the direction of propagation of the tidal wave (Hulscher, 1996). Sand waves are highly dynamic bedforms reaching migration speeds of up to 10 m/yr with an evolutionary timescale of decades.
Coastal seas have a large economic value and are subject to a lot of offshore activities, Figure 1.4 shows an overview of the cables and pipelines on the bottom of the North Sea as well as the sand wave fields. The combination of their dynamic behaviour and wave height may cause them to interfere with offshore activities. For example, sand waves may pose a hazard to navigation, they could move into navigation

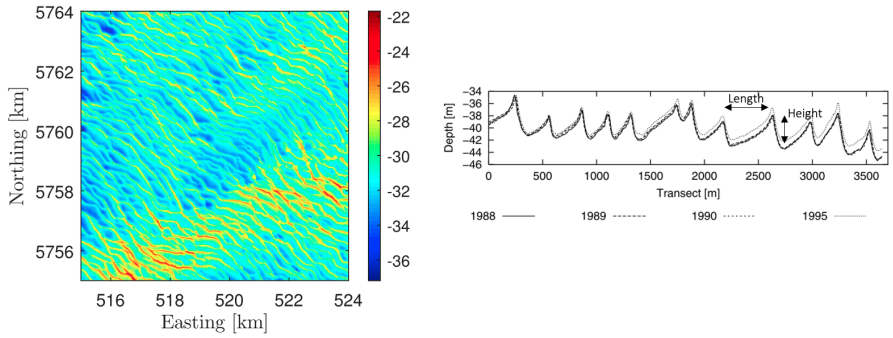

Figure 1.3: Left: bathymetric chart showing a typical sand wave field in the North Sea, depth in m (Campmans, 2018). Right: Seabed profile along a transect of echosounder data of tidal sand waves. Sand waves have an approximate length and height of 300 m and 4 m respectively. The average sand waves migration speed is 6 m/yr (Besio et al., 2004).

channels and reduce the water depth and thereby endanger shipping (Dorst et al., 2013). Furthermore, the safety of pipelines, communication cables and offshore construction depends on the stability of the bed. A buried cable can be exposed due to a migrating sand wave. So far, the problem has been solved by avoidance of sand waves or by burying the object deep enough (Besio et al., 2008). However, this is a very expensive solution and the wide spread appearance of sand waves enhances the need to understand and predict the behaviour of these bedforms. With the help of sand wave modeling, costs can be reduced significantly. Moreover, modeling enhances the understanding of the physical processes behind the formation and migration of sand waves.

A growing need to understand the behaviour of sand waves arises since the Netherlands is planning on building wind farms in order to generate clean and renewable energy. The Dutch government aims that in the year 2030 27% of the consumed energy originates from renewable energy sources. In the year 2050, the consumption of energy should be a 100% renewable. Expected is that in the year 2024 two new wind farms are operational, which will deliver 2.1 GW to the Dutch coast (Rijksoverheid, 2021). Figure 1.4 indicates these wind farms by the red polygons that have a black square around them, these site are called 'Hollandse Kust Zuid' (HKZ) and 'Hollandse Kust Noord' (HKN).

Observations

One of the first observation of sand waves in the North Sea was done by van Veen (1935), where he observed symmetrical sand waves in the southern part of Dutch North Sea. Where the early work of van Veen only focused on the observations of sand waves, McCave (1971) and Terwindt (1971) investigated the role of environmental parameters, such as grain size of the sediment and the current strength, to the occurrence of tidal sand waves. Dorst et al. (2011) looked at the spatial differences in observed sand wave dynamics in the Southern North Sea. Later, the work was extended by identifying the physical processes behind the growth and migration of sand waves by various authors (Besio et al., 2004; van Santen et al., 2011; Damen et al., 2018).

Sand waves are not exclusively observed in the North Sea, they are observed in tidally dominated shallow seas all around the world. In Asia, sand waves are observed in the Taiwan (Zhou, 0118; Boggs, 1974) and in the coastal waters of Japan (Knaapen and Hulscher, 2002; Ikehara and Kinoshita, 1994). In South America sand waves are observed off the coast in Argentina (Aliotta and Perolli, 1987), further up north sand waves are observed in various places, such as Alaska (Bouma et al., 1980), eastern Canada (Duffy and Hughes-Clarke, 2005), eastern US (Perillo and Ludwick, 1984). However, in this thesis the focus is laid on tidally generated sand waves in the North Sea.

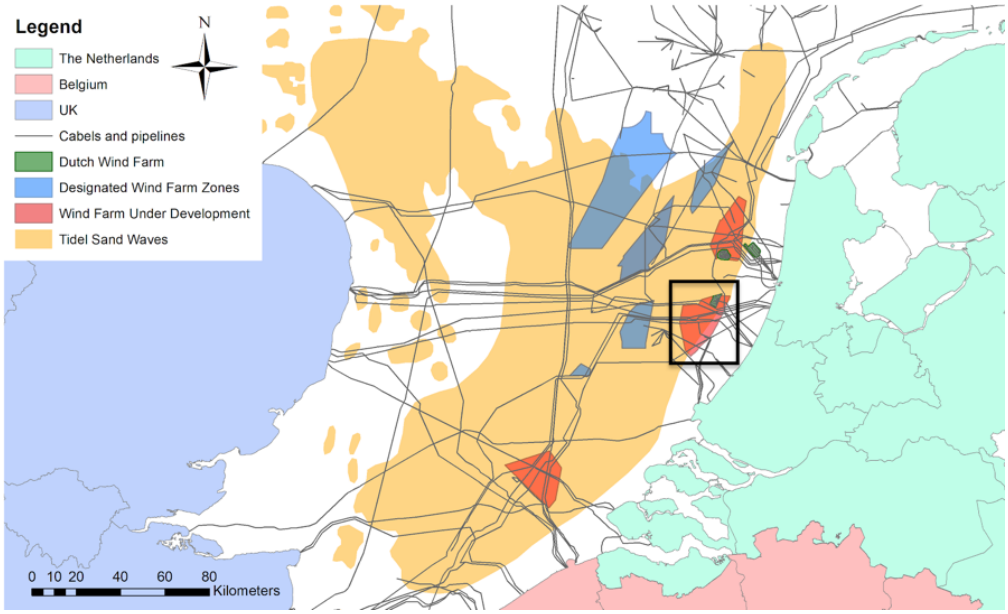

Figure 1.4: Activity map of the North Sea. Sand wave field are indicated with yellow, cables and pipelines are indicated by solid lines. Blue and red planes indicate future wind farms, the location of the 'Hollandse Kust Zuid' wind farm is denoted with a solid square around it (WaterProof 2018).

Physical processes

The formation of sand waves is caused by the interaction of oscillatory tidal flow with bottom perturbations, leading to steady circulating cells in the vertical plane. Figure 1.5 shows a sketch of these recirculating currents over a wavy bottom, it can be seen that there is a convergence (divergence) of the currents above crest (trough) of the perturbation. When currents are strong enough, sediment may be eroded, enabling the perturbations to grow.
When these residual circulation cells are asymmetric (e.g. when the flood flow is stronger than the ebb flow), the areas of convergence (divergences) is shifted with respect to the trough (crest). This results in sand wave migration.

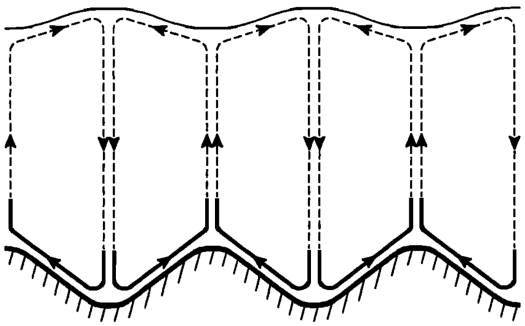

Figure 1.5: Sketch of recirculating currents over bottom undulations (Hulscher, 1996).

1.3 Model background

To understand the formation and the development of tidal sand waves, stability analyses of the flat bottom configuration are commonly used (see the review by Besio et al. (2008)). Small undulations are superimposed on a flat bottom with wavenumber k (= $2\pi/\lambda$, where λ the wavelength). The time development of these undulations are studied by assuming that the perturbations, superimposed on the flat bed, are small. This assumption will allow for linearization of the problem. The applied undulations are of random different spatial scales which, in a linear approximation, will evolve separately. Linear stability analyses assumes that the component characterised by the largest amplification rate will dominate the sea bed after some time. Linear stability analyses also predicts the wavelength and migration speeds of the prevailing bedform. These idealised/exploratory models, which are commonly called linear stability models, are restricted by the small-amplitude assumption. Hence, no information can be gained on the long-term behaviour of the prevailing bedform.
The predictions of the finite-amplitude of the prevailing bedform can be obtained by means of non-linear stability analyses or numerical integration of the full system. These non-linear stability models are based on the assumption that the prevailing bedforms, even of finite-height, are still small in some sense and can be investigated by means of perturbation approach.
Numerical models are complex and are aimed at producing quantitatively accurate results for specific problems. These models offer more flexibility regarding the choices for geometry and other physical processes, making them a powerful tool for engineering applications. Numerical models typically require much computing time, restricting their use to a limited number of model runs within available time. Unlike linear stability models, which are far less CPU hungry.
Both models have their own (dis-)advantages and should be used in combination: the linear stability model to explore relevant processes, and subsequently a numerical model in order to obtain a qualitative accurate result for the identified conditions (e.g. Hommes et al. (2007); Campmans (2018)).

Linear stability models

The first model of sand wave appearance was formulated by Hulscher et al. (1993), which demonstrated that the initial formation of offshore tidal sand waves arise as free instabilities of the coupled water-bottom system. The mechanism bears similarities to that describing sand dunes in rivers (for the latter see Fredsøe (1974) and a recent paper by Vittori and Blondeaux (2020)). Subsequently Hulscher (1996) presented a full 3D hydrostatic model study, in which the residual vertical circulations were explicitly calculated. In this work the the dependence of sand wave characteristics were analysed, i.e., vertical eddy viscosity, A, and bottom slip parameter, s were investigated as well. These parameters relate the turbulence stresses to the mean flow and measure the resistance appearing in the partial slip condition at the sea bed, respectively.

Further improvements of the model concerned the increased complexity in the expression for the closure relation and the hydrodynamics were done by Gerkema (2000); van Santen et al. (2011) and Besio et al. (2003). The later studies apply a 2D vertical approach, which is justifiable as the sand wave orientation is orthogonal to the principle tidal component
These models only considered the growth of sand waves, and not their migration. Németh et al. (2002) and Besio et al. (2004) were the first to develop a linear stability model allowed for sand wave migration, the models that allow for asymmetry in the tidal flow. These models were the first to include, next to the semi-diurnal lunar tide (M2) its first overtide (M4) and a residual current. Here M4 and M0 arise from non-linear processes, M0 also arises due to other physical processes e.g. wind. Furthermore, Campmans et al. (2017) presented a model to study the effect of storms on sand wave formation. It turns out that waves tend to decrease the growth rate of sand waves, because their effect on the downhill gravitational transport component is stronger than their growth-enhancing effect. The effect of wind wave is strongest for wind waves perpendicular to the tidal current, this translate to asymmetrical tidal currents, thus causing sand wave migration.

Nonlinear modelling

The aforementioned models are linear stability models, which are unable to predict the finite-height of sand waves. Németh et al. (2007) presented a model to study the long term behaviour of sand waves. Sand waves were able to a finite height. This work was later extended by van den Berg et al. (2012), where lower computational costs allowed to study a larger domain of wavelengths.

A limitation of idealised models is that they contain only a limited amount of processes. If for example they would be mounted with more sophisticated turbulence closure schemes, solving them requires numerical methods. In such cases, it becomes attractive to use available state-of-the-art numerical morphodynamic models, like Delft3D. Such models offer more flexibility regarding the choices for geometry, turbulence closure, sand transport formulations. Borsje et al. (2013) used a numerical model to simulate the initial formation of sand waves. In this work, different formulations for the closure relations were employed. It turns out than the model overestimates the sand wave length when utilising a constant eddy viscosity profile. van Gerwen et al. (2018) used Delft3D to model sand waves of finite amplitude. He found that the final amplitude of the sand waves was overpredicted compared to the observed sand wave height.

1.4 Knowledge gaps

When models are used to study the initial formation of tidally generated sand waves the eddy viscosity A and the slip parameter s at the bed are kept constant. These parameters are either prescribed (Hulscher et al., 1993; Gerkema, 2000) or calculated from environmental parameters such as the tidal characteristics, depth and the bottom roughness (Besio et al., 2003, 2004). When the parameters A, s are prescribed, they are used as a tuning parameter to model sand wave characteristics which agree with observations. When A and s are obtained through environmental parameters, it turns out that the sand wave characteristics are only in good agreement with observed sand waves when either a too small grain size is used, or when the slip factor is multiplied by a factor of 4 (van Santen et al., 2011). van Santen et al. (2011) makes use of the slip parameter calculated by Besio et al. (2003) and Besio et al. (2004) which is adopted from Hulscher and van den Brink (2001). This indicates that the turbulence closure relation that incorporates the parameters A and s needs to be improved. In this thesis, an improved turbulence model is presented that leads to sand wave characteristics that agree with observations.
Besio et al. (2003) uses the sediment transport formulation described by Meyer-Peter and Müller (1948), where the total bed shear stress is incorporated into the formulation. However, only skin friction, which is part of the total bottom shear-stress, contributes to sediment transport (details given in Section 2.1.3). This indicates that investigation of the influence of the bed-shear stress into the sediment transport formulation is needed.
Furthermore, it is unknown how the results of the linear stability model compares to the numerical model that employs linear stability analyses.

1.5 Research aims

The general aim of this study is to deepen the knowledge and understanding of sand wave characteristics. Specific research aims follow from the knowledge gaps, improving the description for the turbulence closure relations. Furthermore, the focus is laid on the 'Hollands Kust Zuid', since this is one of the locations that is assigned to become a wind farm site. In order to reach these aims, the following research questions are formulated:

1. What would the characteristics of sand waves be for a site specific environment, where the linear stability analyses incorporates an improved turbulence closure model?

2. What is the sensitivity of sand wave characteristics to environmental parameters such as water depth, tidal characteristics and grain size?

3. How do sand wave characteristics computed by different models (linear stability and numerical) compares to each other. How would these model results compare to the observations?

To answer the research questions, an idealized modeling technique is employed. This modeling approach aims to capture the most important mechanisms for sand wave dynamics. To answer the research questions a new formulation for the closure relations is developed. Furthermore, environmental parameters from the HKZ are investigated. The idealized model results are later compared with model results from the state-of-the-art numerical model, Delft3D.

1.6 Outline

The thesis is structured as follows: In Chapter 2 a few general concepts which will be used in the rest of this thesis will be discussed. Chapter 3 discusses the linear stability model along with the numerical model. Next, Chapter 4 describes the model set up for each model and experiments, the environmental data used and how the model outputs are analysed. Finally, Chapter 5 and 6 contain the discussion and conclusions, respectively.

2 General concepts

In this section a few general concepts will be discussed which will be used in the rest of this thesis.

2.1 Sediment transport

2.1.1 Sand and sediment properties

Natural occurring sand consist of a range of individual grains with different grain sizes, d_s. By definition, sediment has a range in grain diameters of 0.062 to 2 mm, finer sediments are classified as clay (Soulsby, 1998). The distribution of certain grain diameters can be analysed by sieving, which results in an accumulation graph (Figure 2.1). The grain-size distribution is usually presented as a curve showing the percentage by mass of grains smaller than d_s, versus d_s. In the figure, the median grain size d_{50} is indicated by the black lines. This measures of sediment is often used in transport calculations.

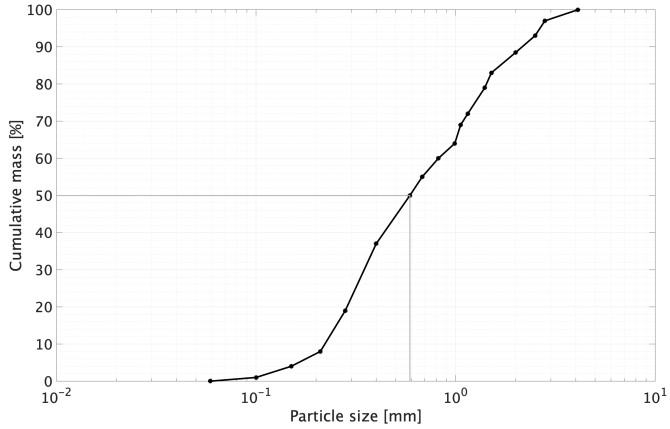

Figure 2.1: Example of grain size distribution (after Soulsby (1998)).

2.1.2 Settling velocity

The settling velocity w_s is the velocity of which suspended sediment falls or sinks towards the bed in calm waters. According to Deigaard and Fredsœ (1992), the drag force F_D on a particle in a fluid is given by

$$F_D = \frac{1}{2} c_D \rho w_s^2 A \,, \tag{2.1}$$

where c_D the drag coefficient, ρ the density of the fluid, w_s the settling velocity and A the area of the particle (projection of the grain upon a plane normal to the flow direction). The drag force is balanced with a counter acting buoyancy and gravitational force F_G,

$$F_G = (\rho_s - \rho)\, g \frac{\pi}{6} d_s^3 \,, \tag{2.2}$$

in which ρ_s denotes the density of sand and g the gravitational acceleration. Under equilibrium conditions the force balance will read

$$(\rho_s - \rho)\, g \frac{\pi}{6} d_s^3 = \frac{1}{2} c_D \rho w_s^2 \frac{\pi}{4} d_s^2 \,, \tag{2.3}$$

which results in the following equation for the settling velocity,

$$w_s = \sqrt{\frac{4\,(\rho_s/\rho - 1)\,g d_s}{3 c_D}}\,. \tag{2.4}$$

The drag coefficient c_D depends on the Reynolds number Re, which is the ratio of inertial forces to viscous forces inside the fluid. For a single spherical particle the grain Reynolds number is

$$Re = \frac{w_s d_s}{\nu}\,, \tag{2.5}$$

in which ν is the kinematic viscosity of the fluid. The relationship of the drag coefficient with the Reynolds number for natural sand follows from Deigaard and Fredsœ (1992) and can be expressed by

$$c_D = 1.4 + 36/Re\,. \tag{2.6}$$

From this expression the analytical expression for the settling velocity w_s can be obtained.

2.1.3 Shear stress, skin friction and bottom roughness

The effects of currents flowing over the bed primarily take place through the friction they exert on the bed, this is expressed in terms of the bed shear-stress. The total bed shear-stress is made up of three components, namely: skin friction (produced by the sediment grains), form drag (produced by the pressure field associated with flow over bed features) and sediment transport (caused by momentum transfer to mobilise grains) (Van Rijn, 1993; Soulsby, 1998). The bed shear-stress is related to the friction velocity u_* by the definition

$$\tau = \rho |u_*| u_*\,, \tag{2.7}$$

The magnitude of the bed shear-stress depends both on the speed of the flow and the roughness of the bed. Within the bottom few meters above the bed the velocity u attains a logarithmic profile

$$u(z) = \frac{u_*}{\kappa} \ln(\frac{z}{z_0}), \tag{2.8}$$

where z is the distance to the bed, z_0 is the bed roughness length and $\kappa \approx 0.4$ is the von Kármán's constant. Equation (2.8) applies to a steady flow without density stratification. Nikuradse (1933) described the bed roughness as

$$z_0 = \frac{k_s}{30}\,, \tag{2.9}$$

where k_s denotes the Nikuradse roughness. In case of a dynamic bed that consist of sediment without any bedform (e.g. ripples) the Nikuradse roughness consist of the grain roughness $k_{s,gs}$ generated by skin friction forces. Several relationships between k_s and the grain size have been proposed, where the one most commonly used depends on the median grain size $k_{s,gs} = 2.5\,d_{50}$. The general formulation of the Nikuradse roughness is the summarised contribution of the following components:

$$k_s = k_{s,gs} + k_{s,r} + k_{s,mr}\,, \tag{2.10}$$

in which $k_{s,r}$ and $k_{s,mr}$ denotes the roughness due to ripples and mega-ripples, respectively. Van Rijn (1991) suggested that the relation of the bottom roughness and the ripples is fixed equal to three times the height of the ripples, Δ_r, where the height of the ripples is assumed to be related to their wave length λ_r, by $0.17\lambda_r$ (Sleath, 1984). The relation between the mega ripples and the roughness originates from Van Rijn (1993) and reads

$$k_{s,mr} = 1.1\Delta_s(1 - \exp(-25\frac{\Delta_s}{\lambda_s}))\,, \tag{2.11}$$

with Δ_s the height of the mega ripples and λ_s their wavelength.

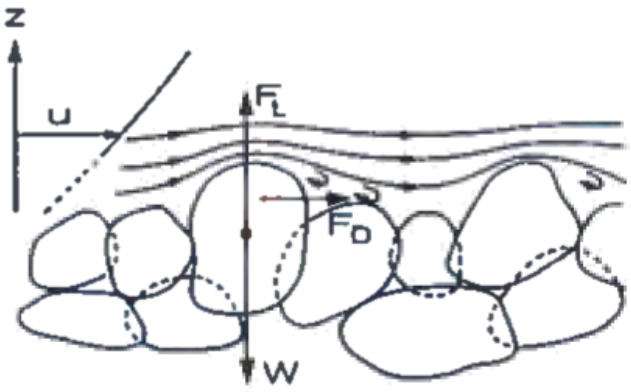

Figure 2.2: Forces acting on a grain of sand, where the stabilizing forces is denoted with W (adopted from Deigaard and Fredsœ (1992)).

2.1.4 Critical bed shear-stress

For sediment particles to start moving a critical bed shear stress has to be reached. This can also be expressed in terms of critical velocity, which is the velocity at which sediment grains will start moving. Shields (1936) determined the threshold of movement based on a ratio between the driving forces F_d and the stabilizing forces F_s, the forces acting on a grain due to a steady horizontal current are shown in Figure 2.2. The driving forces are the horizontal drag force F_D and the lift force F_L, which result from the friction and pressure differences along the grains surface. The stabilizing force F_S is due to gravitational effects and is also called the weight of the submerged particle. The horizontal drag force on a grain particle with diameter d_s is given by

$$F_D = \frac{1}{2}\rho c_H \frac{\pi}{4} d_s^2 U^2 \,, \tag{2.12}$$

c_H the drag coefficient related to the relative roughness and U represents the horizontal flow velocity. The lift force that a grain experiences is due to the flow that is disturbed by the particle itself, leading to deflection of the stream lines over the top of the grain particle (figure 2.2). The deflection of the stream lines results in acceleration of the fluid over the top of the grain particle, leading to vertical pressure differences over the grain (Dyer, 1986). The lift experienced by the grain is

$$F_L = \frac{1}{2}\rho c_L \frac{\pi}{4} d_s^2 U^2 \,, \tag{2.13}$$

with c_L the lift coefficient. The two driving forces can be combined into the total driving force

$$F_d = \frac{1}{2}\rho c_T \frac{\pi}{4} d_s^2 \left(\alpha u_*\right)^2 \,, \tag{2.14}$$

with c_T including both the drag and lift coefficient αu_* the friction velocity at the distance of the order of magnitude d_s from the bed.
The stabilizing force F_S can be modelled as frictional force acting on a sediment grain. For a non-moving grain the stabilizing force is given by

$$F_S = \rho g(\rho_s/\rho - 1)\frac{\pi}{6} d^3 \tan(\phi_r) \,. \tag{2.15}$$

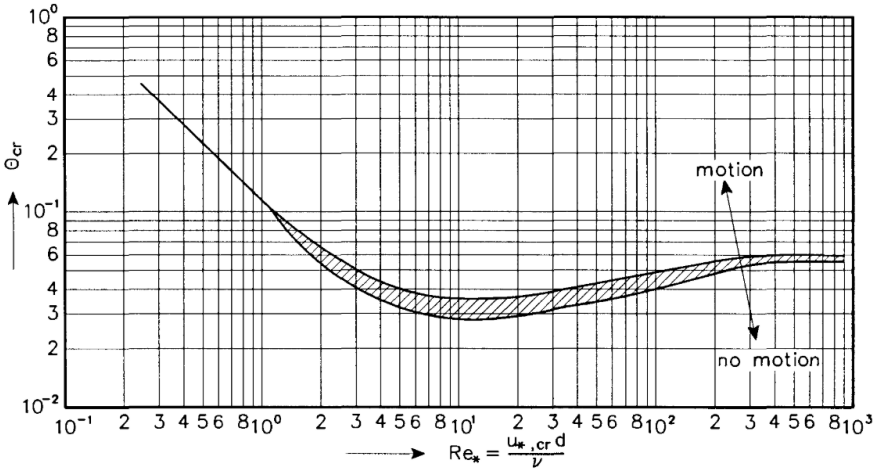

Figure 2.3: The Shields curve showing the critical Shields parameter θ_c as a function of the grain Reynolds number Re. For Shield parameter θ larger than θ_c (curve), the grain particles start to move. From Van Rijn (1993).

Here $\tan \phi_r$ is the measure for the maximum friction between the grain and the surrounding grains, ϕ_r is the angle of repose for the sediment. The critical friction velocity u_{*c} is determined by the balance of the driving force and stabilizing force, which becomes after some rewriting

$$\frac{u_{*c}^2}{(\rho_s/\rho - 1)gd_s} = \frac{4 \tan \phi_r}{3c_d \alpha} \tag{2.16}$$

The parameter on the left-hand-side is the critical Shields parameter θ_c. The critical friction velocity is related to the critical bed shear-stress τ_c via expression 2.7. The critical Shields parameter in terms of critical bed shear-stress is

$$\theta_c = \frac{\tau_c}{(\rho_s - \rho)\, g d_s} \tag{2.17}$$

Shields (1936) found a weakly dependence of the value of the critical Shields parameter on grain Reynolds number Re, which is defined as

$$Re = \frac{u_* d_s}{\nu}\,, \tag{2.18}$$

with ν the kinematic viscosity of the fluid. Figure 2.3 shows the Shields curve as a function of the grain Reynolds number, it can be seen that value for the critical Shields parameter attains a constant value of $\theta_c = 0.047$ for larger values of the particle Reynolds number (Van Rijn, 1993). The sediment will be set in motion when the value for the Shields parameter exceeds the critical value for the Shields parameter.

2.1.5 Transport mechanisms

Modes of transport

When the Shields parameter exceeds the critical value for the Shields parameter the sediment can be transported in different ways, as bed load transport, as suspended load transport and as a combination of the two. In bed load transport the sediment moves through sliding, rolling and saltating. In suspended load the sediment move because they are in suspension in the water column, both modes of transport are shown in Figure 2.4.
When the sediments moves as bed load the sediment starts to roll and bounce over the bed. The sediment

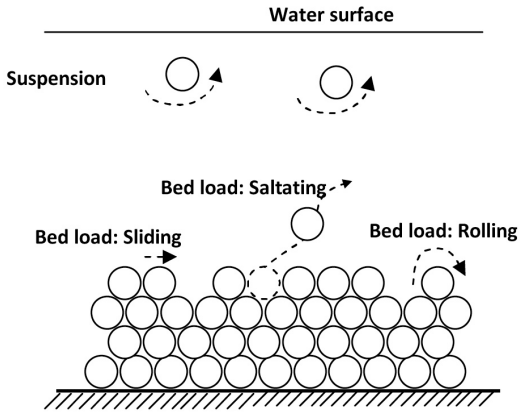

Figure 2.4: Sketch of three typical modes of bed load and suspended load by Gao (2010).

is almost constantly in contact with the bed and is very responsive to any changes in the velocity. The transport of sand is calculated by multiplication of the sand concentration and the flow velocity. In case of bed load, the concentration of sediment is approximately proportional to the shear stress τ (Soulsby, 1998), which is proportional to the velocity squared via equation 2.7. Therefore, a good estimate of bed load transport is proportional to the friction velocity cubed

$$|\overrightarrow{Q_b}| \propto |\overrightarrow{u_*}^3| \,. \tag{2.19}$$

When the friction velocity is approximately equal to the fall velocity of the grains $w_s/u_* \approx 1$, the sediment is suspended and is no longer in contact with the bed. Once the particles are suspended most of the turbulent forces are the same or larger than the submerged weigh the particles, the particles stay suspended (Van Rijn, 1993). The particles move approximately with the velocity of the flow. The suspended sediment transport Q_s is obtained by integrating the flow velocity and the suspended sediment concentration over the whole water column,

$$\overrightarrow{Q_s} = \int \vec{u}(z)c(z)\mathrm{d}z \,, \tag{2.20}$$

with c is the volumetric concentration of suspended sand.

2.2 Sand wave dynamics

The physical mechanisms underlying the formation of sand waves are described in section 2.2.1, section 2.3 explains the procedure to capture the initial dynamics of sand waves in a linear stability model.

2.2.1 Formation

Sand waves arise from the interaction of the bottom with the tidal currents. The hydrodynamic response on perturbation of the bottom can be best explained by considering the description of headland eddies by Zimmerman (1981). The same mechanisms creating the headland eddies are responsible for creating the residual circulations over bottom perturbations. However, the hydrodynamic response in the vertical plane is analysed rather than the response in the horizontal plane.
When the tidal flow encounters a perturbation, the flow at a fixed level will accelerated moving up the slope and decelerated moving down the slope. Whilst the flow accelerates, a frictional boundary layer will develop close at the bed, in which the velocity decreases towards zero. This will result in a production

of vorticity. Figure 2.5 shows a tidal flow that encounters a perturbation. First consider the flood phase, which is denoted with the red arrows, the flow produces a clockwise vorticity on the upstream side of the perturbation. Due to the increased flow velocities at the crest, the production of vorticity is larger at this location. The clockwise vorticity is transported towards the right by the tidal current, resulting in a convergence of clockwise vorticity to the right of the perturbation and a divergence of clockwise vorticity to the left.
During the ebb phase, which is denoted with the blue arrows, the flow is now directed into the opposite direction. The flow now produces an anticlockwise vorticity, which is advected towards the left. Now, a convergence of anticlockwise vorticity to the left of the perturbation and a divergence of anticlockwise vorticity at the right. Averaging over one tidal cycle, there is a net generation of vorticity on both sides of the perturbation with opposite signs. This results in larger residual circulation cells, these are shown by the black solid lines in Figure 2.5.

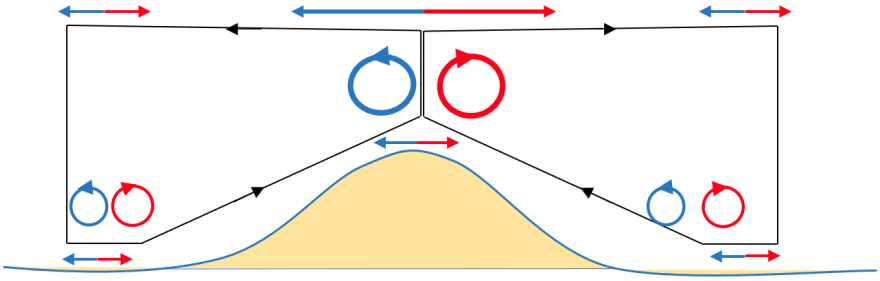

Figure 2.5: Schematic of residual circulation induced by an oscillatory tidal flow over a sand wave. Tidal currents in ebb and flood phase are represented by blue and red arrows, respectively. The solid black cell represents the net residual circulation. (adapted after Zimmerman (1981)).

Response of sediment to the residual circulation

In figure 2.5 it is shown that the residual circulation cells converge at the top of the perturbation, diverging from the troughs. Consider a net transport of sediment due to the recirculating currents, transporting sediment from the troughs towards the crests, leading to growth of the amplitude of the bottom perturbation. The growth of the perturbation is limited due to the gravitation force acting on the sediment grains located on the slope of the perturbation, resulting in a fall of the sediment grain towards the trough. This effect will become more apparent when the wavelength of the perturbation small due to the increased angle of the slope.

Sand wave migration

So far only a symmetrical tidal flow, where the peak ebb current equals the peak flood current, over a perturbation has been considered. When asymmetry is present the peak ebb current will not be equal to the peak flood current, leading to a displacement of the residual circulation cells. These displaced cells with respect to the crest will lead to a displaced convergence of sediment, eventually leading to a shift or migration of the bottom perturbation. Asymmetries in the tides are discussed in a separate subsection.

2.2.2 Tidal asymmetry

Asymmetry in the forcing can emerge when either the peak flood amplitude/duration differs from the peak ebb amplitude/duration, or the duration of the transition from ebb to flood differs from the duration of the transition from flood to ebb. The emerging asymmetry can be due to the presence of residual currents or

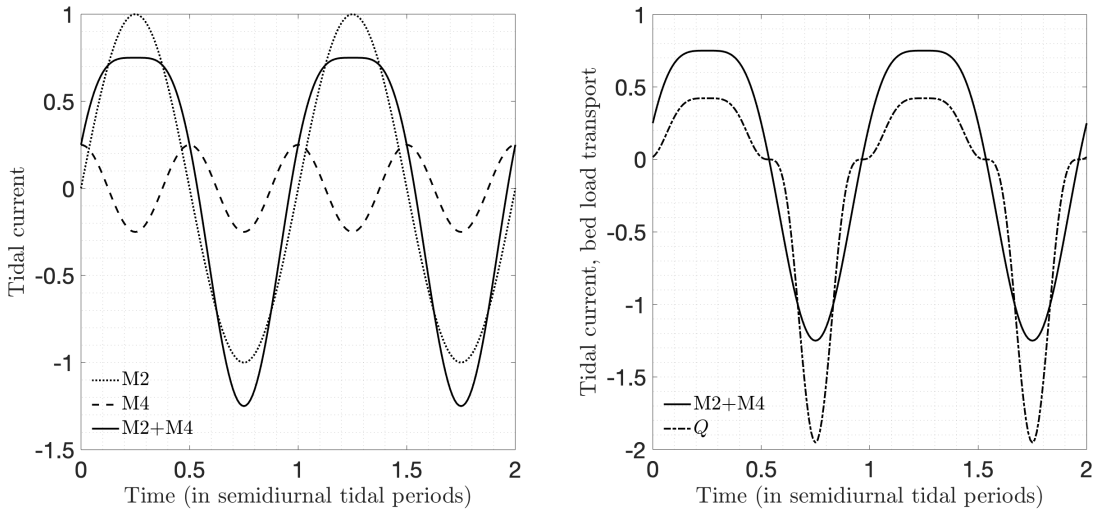

Figure 2.6: (left) Superposition of the tidal current M2 and its first overtide M4 for a phase difference of $\phi = \pi/2$. (right) Bed load transport $Q \propto \alpha u^3$ with $\alpha = 1\ \mathrm{s^2 m^{-1}}$.

due to overtides (Gerkema, 2019). When the superposition of the most dominant tide (M2) in the North sea and its overtide (M4) is considered, the velocity can be written as

$$u = A_{\mathrm{M2}} \sin(\sigma_{\mathrm{M2}} t) + A_{\mathrm{M4}} \sin(2\sigma_{\mathrm{M2}} t + \varphi)\ . \tag{2.21}$$

Here, A_{M2} and A_{M4} are the amplitudes of the M2 and M4 tidal constituents, respectively. The angular frequency corresponding to the M2 tide is denoted by σ_{M2}, φ is the phase difference between the tidal constituents. Figure 2.6 shows an example of asymmetrical tides and the resulting bed load transport. In the figure the amplitudes of M2 and M4 are taken to be $A_{\mathrm{M2}} = 1\ \mathrm{m\,s^{-1}}$ and $A_{\mathrm{M4}} = 0.25\ \mathrm{m\,s^{-1}}$ with a phase difference of $\varphi = \pi/2$. Here positive (negative) values for the tidal currents represents the flood (ebb) phase. It can be seen that a superposition of the tidal current M2 and its first overtide M4 leads to an assymetrical tide that favours the ebb phase. Figure 2.6 also shows the sediment transport due to the tidal currents, here is considered that sediment transport is approximately proportional to the velocity cubed (equation 2.19). It can be seen that sediment is transported is stronger during the ebb phase.

2.3 Stability analyses

The initial formation of tidally generated sand waves is usually computed by means of linear stability analyses. Here a model computes the temporal development of the initial bottom amplitude, resulting in expression that quantifies the growth and migration of the bottom. In Section 3, a description of both an numerical model and a simple model is given. Section 3.1.6 shows that the temporal development of the initial bottom amplitude is given by

$$\Gamma = \Gamma_r - i\Gamma_i \tag{2.22}$$

where the real part Γ_r controls the amplification/decay of the bottom perturbation while, the imaginary part, Γ_i relates to their migration. In order to identify the behaviour of a range sand wavelengths, the model computes the growth and migration rates for a range of initial perturbations k. It is assumed that the actual sand waves are generated by the growth of the bottom perturbation with the largest amplification rates, the sand waves with this wavelength will dominate the bottom topography. The maximum amplification rate is called the fast growing mode which corresponds to a certain wave number, k_{fgm}. In order to find the

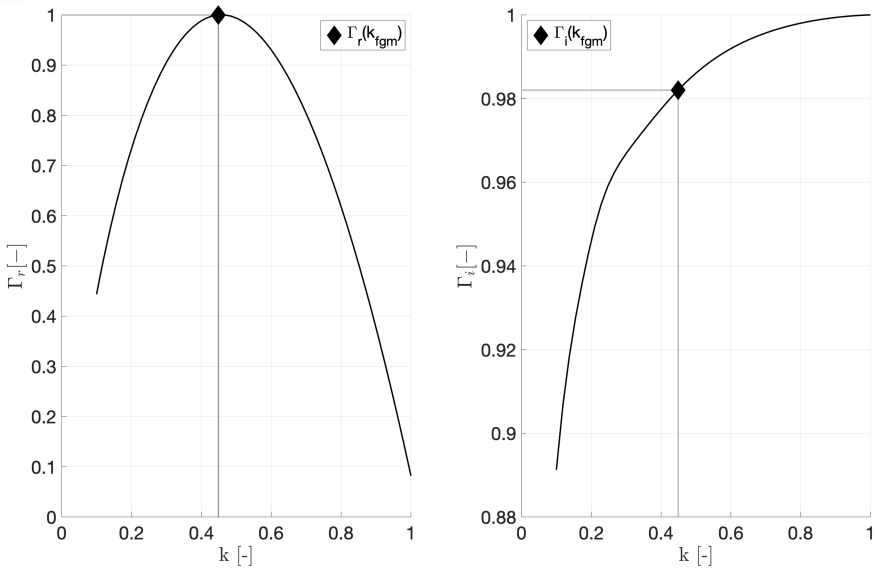

Figure 2.7: Procedure of selecting the fast growing mode in the linear stability model. The value for Γ_r controls the amplification/decay of the bottom perturbation, where it is assumed that $\Gamma_r(k_{\mathrm{fgm}})$ will dominate the sea bed topography. The wave number k_{fgm} corresponds to migration of this mode: $\Gamma_i(k_{\mathrm{fgm}})$.

corresponding value for the migration, the imaginary part of Γ_i $k = k_{\mathrm{fgm}}$ is calculated. A non-dimensional example of the selection of the fast growing mode and the corresponding migration rates is shown in Figure 2.7. The wavelength λ of the sand waves is $\lambda = 2\pi/k_{\mathrm{fgm}}$ and the migration speed is $\Gamma_i(k_{\mathrm{fgm}})$. There is no exact definition until when the linear stability analyses holds, but a commonly used measure is the e-folding time. This is the time over which the initial amplitude increases by a factor e, the e-folding time is $1/\Gamma_r(k_{\mathrm{fgm}})$ (Dodd et al. (2003)).

3 Models

In order to answer the research questions introduced in Section 1.5 two different models have to be employed. The different models used are:

- Linear stability model
- Numerical model

In this chapter, the linear stability model is discussed in Section 3.1 and the numerical model in Section 3.2. Firstly, the domain of the simple linear stability model is discussed (Section 3.1.1), followed by the formulation of the problem (Section 3.1.2), the basic state (Section 3.1.3) and the time development of the bottom perturbations (Section 3.1.4). Finally in Section 3.1.5 and Section 3.1.6 the hydrodynamic and morphodynamic response are discussed, respectively. The section on the numerical model describes the hydrodynamics (3.2.1) and the morphodynamics (Section 3.2.2).

3.1 Linear stability model

3.1.1 Domain

The linear stability model used is an extension of the model described by Besio et al. (2003, 2004). The model simulates the feedback between a tidally driven flow, sediment and a sandy bottom in an offshore part of a shallow continental shelf, with no nearby lateral boundaries. A 2-dimensional Cartesian coordinate system is considered where the x-, z-axes are pointing in the horizontal and vertical direction, respectively. A sketch of the model geometry is given in Figure 3.1.

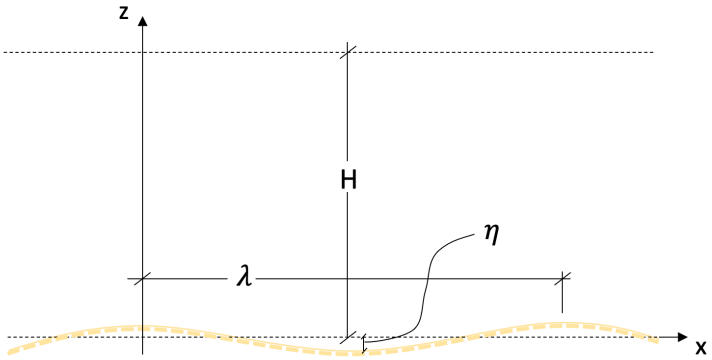

Figure 3.1: Model geometry, showing a coordinate system with the water depth H, the bed level $\eta(x,t)$ and the wavelength of the sand wave, λ.

3.1.2 Formulation of the problem

Consider a tidally generated flow over a cohesionless bed. The flow can be described in a two-dimensional system where after applying the Boussinesq approximation and Reynolds-averaging the hydrodynamics of the model can be described by

$$\frac{\partial \boldsymbol{u}}{\partial t} + (\boldsymbol{u} \cdot \nabla)\boldsymbol{u} = -\frac{1}{\rho}\nabla P + A\nabla^2 \boldsymbol{u}\,, \tag{3.1}$$

$$\nabla \cdot \boldsymbol{u} = 0\,. \tag{3.2}$$

With $\boldsymbol{u} = (u, w)$ the horizontal and vertical velocity components, respectively, ∇ is the gradient operator $(\partial/\partial x, \partial/\partial z)$, ρ the density of the water, P the pressure and A represents the eddy viscosity. At the bed $(z = \eta(x,t))$, the partial slip condition is applied:

$$\frac{\partial u_{||}}{\partial n} = \tilde{s} u_{||} \quad \text{at} \quad z = \eta(x,t)\,. \tag{3.3}$$

Here the $\partial/\partial n$ represents the derivative in the direction normal to the bed and $u_{||}$ the alongslope velocity component and $\tilde{s}$ the stress parameter. Gerkema (2000) defines the alongslope velocity component as

$$u_{||} = \frac{u + \frac{\partial \eta}{\partial x} w}{\sqrt{1 + \frac{\partial \eta^2}{\partial x}}}\,. \tag{3.4}$$

At the surface $(z = H)$, the rigid lid approximation is applied, here waves and wind are not taken into account. So imposed at $z = H$ is no vertical velocity and no shear:

$$w = 0, \quad \frac{\partial u}{\partial z} = 0 \quad \text{at} \quad z = H\,. \tag{3.5}$$

The morphodynamics of the model is governed by the sediment continuity equation, which states that a convergence (divergence) of the sediment results in a rise (fall) of the bed level:

$$\frac{\partial \eta}{\partial t} + \frac{\partial Q}{\partial x} = 0\,. \tag{3.6}$$

where Q denotes the sediment flux per unit width divided by a porosity factor. To allow for an easy comparison with Besio et al. (2003) we follow his analyses and impose the sediment transport formulation described by Meyer-Peter and Müller (1948)

$$Q = 8 \frac{\sqrt{(\rho_s/\rho - 1) g d_{50}^3}}{1 - p} \cdot \left(\left| \theta - \gamma \frac{\partial \eta}{\partial x} \right| - \theta_{\text{crit}} \right)^{3/2} \cdot \left(\theta - \gamma \frac{\partial \eta}{\partial x} \right) \cdot \left| \theta - \gamma \frac{\partial \eta}{\partial x} \right|^{-1}, \tag{3.7}$$

where ρ_s is the density of sand, ρ the density of the water, g the acceleration due to gravity, d_{50} is the median grain size, p the porosity factor and θ the Shields parameter, with the critical Shields parameter $\theta_{\text{crit}} = 0.047$. The term $\gamma \frac{\partial \eta}{\partial x}$ has been added, as suggested by Fredsøe (1974), in order to take the bedslope effect into account. In this expression there is only transport of sediment when the term $\left|\theta - \gamma \frac{\partial \eta}{\partial x}\right|$ is larger than the critical Shields parameter, θ_{crit}.

In this work two different methods are employed in order to obtain values for the eddy viscosity A and stress parameter $\tilde{s}$. One method follows from the procedure of Hulscher and van den Brink (2001), combined with the knowledge of the turbulence structure and eddy viscosity in steady currents. The procedure of Hulscher and van den Brink (2001) equates A to the depth-averaged value of empirical relation proposed to describe the kinematic eddy viscosity and forcing the shear stress acting on the bed to be equal to $\rho \frac{U_m}{C}^2$. Here the shear stress has a dependency on the conductance coefficient C, which is dependent on the bottom, it turns out that

$$A = \frac{\kappa U_m H}{6C}, \quad \tilde{s} = \frac{6}{H(\kappa C - 2)}, \quad C = 2.5 \ln\left(\frac{H}{k_s}\right) + 6\,. \tag{3.8}$$

Here κ is the von Kármán constant, k_s is the bottom roughness described in section 2.1.3 and U_m is the depth-averaged velocity in the absence of bottom undulations

$$U_m = \frac{1}{H} \int_0^H u(z)\, dz\,. \tag{3.9}$$

The other method employed to obtain values for the eddy viscosity A and stress parameter $\tilde{s}$ follows from personal communication with Prof. Huib de Swart (2020). The method incorporates a log-layer near the bottom where the vertical flow profile is assumed to be logarithmic. Derivation of the eddy viscosity and stress parameter can be found in appendix A, which yields the following expressions:

$$A = k|u_*|(\delta_l + z_0)(1 - \frac{\delta_l}{h}), \quad s = \frac{1}{\delta_l + z_0} \frac{1}{\ln\left(\frac{\delta + z_0}{z_0}\right)}. \tag{3.10}$$

Note that these parameters are dependent on the height of the log-layer δ_l, which attains a value of 1.44m for the HKZ environment.

3.1.3 The basic state

As the basic state a unidirectional tidal flow is taken over a flat bottom, the flow ($u = u_b(t, z)$, $w = 0$) is assumed to be driven by an oscillatory horizontal pressure gradient p of angular frequency σ

$$\frac{\partial p}{\partial x} = -P_{0x} - \sum_{n=1}^{2} \frac{P_{nx}}{2}(e^{in\sigma t} + c.c.). \tag{3.11}$$

Here P_{1x} and P_{2x} are complex amplitudes of the oscillatory pressure gradient of the semi-diurnal (M2) and quarter-diurnal (M4) tidal wave constituents, respectively, and P_{0x} is a constant. The horizontal momentum equation reduce to

$$\frac{\partial u_b}{\partial t} = -\frac{1}{\rho}\frac{\partial p}{\partial x} + A\frac{\partial^2 u_b}{\partial z^2}, \tag{3.12}$$

along with the boundary conditions (3.3) and (3.5):

$$\frac{\partial u_b}{\partial z} = \tilde{s}u_b \quad \text{at} \quad z = 0, \quad \frac{\partial u_b}{\partial z} = 0 \quad \text{at} \quad z = H. \tag{3.13}$$

Plugging in the expressions for u_b and p_x, solving the differential equation and applying the boundary conditions, results in the solution for the basic state. The derivation is given in the appendix B, which yields

$$u_b(z,t) = -\frac{P_{0x}}{\rho A_V}\left(\frac{z^2}{2} - Hz - \frac{H}{\tilde{s}}\right) + \left[\sum_{n=1}^{2} \frac{P_{nx}}{2ni\rho\sigma}\left(1 + \tilde{c}_n\left(E_n^2 e^{-(i+1)\frac{z}{\Delta_n}} + e^{(1+i)\frac{z}{\Delta_n}}\right)\right)e^{in\sigma t} + c.c.\right] \tag{3.14}$$

Here, Δ_n is a viscous length defined in terms of the eddy viscosity A and of the angular frequency of the tidal oscillation σ,

$$\Delta_n = \sqrt{\frac{2A}{n\sigma}}, \quad E_n = e^{(1+i)\frac{H}{\Delta_n}}, \quad \tilde{c}_n = -\frac{\tilde{s}}{\tilde{s}(E_n^2 + 1) + (1+i)(E_n^2 - 1/\Delta_n)}. \tag{3.15}$$

By integrating equation (3.14) over the depth, amplitudes of the depth averaged velocity oscillations are obtained,

$$\left|\hat{U}_{0_m}\right| = \frac{|P_{0x}|}{\rho A}\left(\frac{H^3}{3} + \frac{H^2}{\tilde{s}}\right) \tag{3.16}$$

$$\left|\hat{U}_{n_m}\right| = \frac{|P_{nx}|}{\rho\sigma}\left|1 + \tilde{c}_n\frac{(\Delta_n/H)}{(1+i)}\left(E_n^2 - 1\right)\right| \tag{3.17}$$

Gerkema (2000) argues that for moderate values for the parameter $\mu(= H^2/(A/\sigma))$, which is the square of the ratio between the water depth and the viscous length, the basic flow due to the M2 tidal component can be approximated as follows,

$$u_b = \frac{1}{2}U_0\big(z_c + \frac{z}{H}\big)\big(2 + z_c - \frac{z}{H}\big)e^{i\phi}e^{i\sigma t} + c.c.\,, \tag{3.18}$$

where z_c is a dimensionless constant defined as:

$$z_c = -1 + \sqrt{1 + 2/\tilde{s}H}\,. \tag{3.19}$$

By applying this approximation, a velocity scale and fitting parameters are introduced, where U_0 and ϕ can be obtained by comparing the exact solution of the basic flow (3.14) with the approximated basic flow (3.18). It turns out that

$$U_0 = \frac{U_m}{[\frac{2}{3} + z_c(2 + z_c)]}\,, \tag{3.20}$$

where U_m is the amplitude of the depth averaged velocity oscillation induced by the M2 tidal component, which can be retrieved from Eq. (3.14). Note that U_m is proportional to P_{2x}.

3.1.4 Time development of the bottom perturbations

The next step in order to analyse the linear stability is to perturbed the basic state by introducing an infinitesimal topography with an arbitrary wave number k. Because the amplitudes are small, the problem can be linearized. The bottom perturbations are of the form

$$\eta(x,t) = \Pi(t)\cos(kx) = \frac{1}{2}\Pi(t)e^{ikx} + c.c.\,, \tag{3.21}$$

here Π describes the long-term evolution and is assumed to be much smaller than H. The flow field now consists of two: the basic flow and the perturbed flow. In terms of their stream function ψ, such that $u = \partial\psi/\partial z$ and $w = -\partial\psi/\partial x$, the total flow can be written as

$$(u, w) = (u_b, 0) + \left(\frac{\partial\psi}{\partial z}, -\frac{\partial\psi}{\partial x}\right). \tag{3.22}$$

Plugging the expressions for the perturbed flow into the momentum equation (3.1) gives (note that in Eq. (3.23)-(3.26) derivatives are indicated as subscript);

$$u_{b,t} + \psi_{zt} + (u_b + \psi_z)\,\psi_{xz} - \psi_x\left(u_{b,z} + \psi_{zz}\right) = -\frac{1}{\rho}p_{b,x} - \frac{1}{\rho}p'_x + A_v u_{b,zz} + A_v\psi_{zxx} + A_v\psi_{zzz} \tag{3.23}$$

$$-\psi_{xt} - (u_b + \psi_z)\,\psi_{xx} + \psi_x\psi_{xz} = -\frac{1}{\rho}p_{b,z} - \frac{1}{\rho}p'_z - A_v\psi_{xxx} - A_v\psi_{xzz} \tag{3.24}$$

After linearization the equations (3.23) and (3.24) become:

$$\psi_{zt} + u_b\psi_{xz} - u_{b,z}\psi_x = -\frac{1}{\rho}p'_x + A_v\psi_{zxx} + A_v\psi_{zzz} \tag{3.25}$$

$$-\psi_{xt} - u_b\psi_{xx} = -\frac{1}{\rho}p'_z - A_v\psi_{xxx} - A_v\psi_{xzz} \tag{3.26}$$

In order to eliminate the (perturbed) pressure gradients in (3.25)-(3.26) the vorticity equation is derived by taking the z-derivative of equation (3.25) and the x-derivative of (3.26) and subtract the two, which results in the following vorticity equation

$$\frac{\partial}{\partial t}\nabla^2\psi + u_b\frac{\partial}{\partial x}\nabla^2\psi - \frac{\partial^2 u_b}{\partial z^2}\frac{\partial\psi}{\partial x} = A\nabla^4\psi\,, \tag{3.27}$$

where $\nabla^2 = \partial^2/\partial x^2 + \partial^2/\partial z^2$. The boundary conditions (3.3) and (3.5) in terms of ψ and after linearization become:

$$\frac{\partial\psi}{\partial x} + u_b\frac{\partial\eta}{\partial x} = 0\,, \quad \frac{\partial^2\psi}{\partial z^2} + \frac{\partial^2 u_b}{\partial z^2}\eta = \tilde{s}\left(\frac{\partial\psi}{\partial z} + \frac{\partial u_b}{\partial z}\eta\right) \quad \text{at} \quad z = 0\,, \tag{3.28}$$

$$\frac{\partial\psi}{\partial x} = 0\,, \quad \frac{\partial^2\psi}{\partial z^2} = 0 \quad \text{at} \quad z = H\,. \tag{3.29}$$

In order to solve the mathematical problem, it is convenient to make (3.27) dimensionless. The dimensionless parameters denoted by an apex, where the inverse of the wave number k^{-1} is used as the horizontal length scale and the water depth H is used for the vertical length scale. The velocity scales with U_0 and the time with σ^{-1}. The sediment transport scales with the quantity $\sqrt{(\rho_s/\rho - 1)g d_{50}^3}$. The dimensionless morphodynamic time scales with T'. The scaled variables

$$x' = kx\,, \quad z' = z/H\,, \quad t' = \sigma t\,, \tag{3.30}$$

$$u_b' = u_b/U_0\,, \tag{3.31}$$

$$\eta' = \eta/H\,, \quad \Pi' = \Pi/H\,, \quad \psi' = \psi/(U_0 H)\,, \tag{3.32}$$

$$T' = t\sqrt{(\rho_s/\rho - 1)g d_{50}^3}/[(1-p)H^2]\,. \tag{3.33}$$

The amplitude U_0 is used for scaling the velocities, where U_0 is given by equation (3.20). The time t has been made dimensionless in two ways: (1) by tidal frequency σ and (2) by morphodynamic timescale T'. The choice of two different timescales is justified because the flow field changes over timescale t, which is much shorter than the time scale of bottom development T'. Because of the two different timescales, the hydrodynamic equation can be decoupled from the one describing the development of the bottom perturbations. For convenience, the apexes of the scaled variables will be dropped from hereon. Using the scaled variables, as well as making use of the spatial structure of bed level η, the stream function can be written as

$$\psi(x,z,t) = \Pi(T)\Psi(z,t)e^{ix} + c.c.\,. \tag{3.34}$$

Plugging in the expression for the dimensionless stream function (3.34) into the (3.35) gives

$$\frac{1}{r}\frac{\partial}{\partial t}(N^2\Psi) + iu_b N^2\Psi - i\Psi\frac{\partial^2 u_b}{\partial z^2} = \frac{1}{\mu r}N^4\Psi \tag{3.35}$$

along with the scaled boundary conditions

$$\Psi + \frac{1}{2}u_b = 0\,, \quad \frac{\partial^2\Psi}{\partial z^2} + \frac{1}{2}\frac{\partial^2 u_b}{\partial z^2} = s\left(\frac{\partial\Psi}{\partial z} + \frac{1}{2}\frac{\partial u_b}{\partial z}\right) \quad \text{at} \quad z = 0\,, \tag{3.36}$$

$$\Psi = 0\,, \quad \frac{\partial^2\Psi}{\partial z^2} = 0 \quad \text{at} \quad z = 1\,. \tag{3.37}$$

In (3.35) the derivatives of Π has been neglected because the morphodynamic time scale is much larger than the hydrodynamic timescale. The operator N^2 in (3.35) is defined as $N^2 = \partial^2/\partial z^2 - \delta^2$. The dimensionless parameters

$$\delta = kH, \quad r = kU_0/\sigma, \quad \mu = H^2\sigma/A, \quad s = \tilde{s}H, \quad \gamma. \tag{3.38}$$

The parameter δ is the dimensionless wave number of the bottom perturbation. Here the value of δ is expected to be in the order of one, since the sand waves have a typical length scale of the order of 100m and the water depth is of tens of meters. The parameter r is similar to the Keulegan-Carpenter number, which is a measure of the ratio of the tidal excursion length and the wavelength of the bottom perturbation. μ is an inverse Stokes number, s is a dimensionless stress parameter and γ a bed slope coefficient. Finally, after averaging over one tidal cycle, the time development of the bottom perturbation is described by

$$\frac{\partial \Pi}{\partial T} + 2\delta i \langle Q \rangle \Pi = 0\,, \tag{3.39}$$

$$Q = 12\left[\left|\frac{\delta\Psi_d}{\mu r}\frac{\partial u_b}{\partial z}\right|_{z=0} - \theta_c\right]^{1/2}\left[\frac{\delta\Psi_d}{\mu r}\left(\frac{\partial^2\Psi}{\partial z^2} + \delta^2\Psi + \frac{1}{2}\frac{\partial^2 u_b}{\partial z^2}\right)_{z=0} - \frac{i\gamma\delta}{2}\right]. \tag{3.40}$$

Here, the brackets $\langle\rangle$, denotes the time average over one tidal cycle, Ψ_d is defined as

$$\Psi_d = \frac{U_0^2}{(\rho_s/\rho - 1)g d_{50}}\,. \tag{3.41}$$

The rest of the analyses consist of two parts. First, the hydrodynamic response to the bottom perturbations has to be calculated, that is done by solving Ψ from (3.35) subjected to the boundary conditions (3.36) and (3.37). Once Ψ has been found, the morphological response can be obtained by substituting Ψ in (3.40), and performing the averaging procedure over one tidal cycle of (3.39).

3.1.5 The hydrodynamic response

The hydrodynamics are solved by methods similar to the procedure employed by Vittori (1989) and Besio et al. (2003, 2004). This procedure exploits the fact that the basic flow is periodic in time which allows for the stream function Ψ to be expanded as a Fourier series in time,

$$\Psi = \sum_{n=-\infty}^{\infty} \hat{\Psi}_n(z) e^{in\sigma t}\,. \tag{3.42}$$

Then, substituting (3.42) into the hydrodynamic expression (3.35) along with the boundary conditions (3.36) and (3.37) gives the following set of coupled linear ordinary differential equations:

$$\frac{in}{r}N^2\hat{\Psi}_n + i[\hat{U}N^2\hat{\Psi}_{n-1} + \hat{U}^*N^2\hat{\Psi}_{n+1}] - i\left[\frac{d^2\hat{U}}{dz^2}\hat{\Psi}_{n-1} + \frac{d^2\hat{U}^*}{dz^2}\hat{\Psi}_{n+1}\right] = \frac{1}{\mu r}N^4\hat{\Psi}_n\,, \tag{3.43}$$

along with the following boundary conditions

$$\hat{\Psi}_n = 0\,, \quad \frac{d^2\hat{\Psi}_n}{dz^2} = 0 \quad \text{at} \quad z = 1\,, \tag{3.44}$$

$$(\hat{\Psi}_n, \hat{\Psi}_1, \hat{\Psi}_{-1}) = \left(0, -\frac{\hat{U}}{2}, -\frac{\hat{U}^*}{2}\right) \quad \text{at} \quad z = 0\,, \tag{3.45}$$

$$\left(\frac{d^2}{dz^2} - s\frac{d}{dz}\right)(\hat{\Psi}_n, \hat{\Psi}_1, \hat{\Psi}_{-1}) = \left(-\frac{1}{2}\frac{d^2}{dz^2} - s\frac{d}{dz}\right)(0, \hat{U}, \hat{U}^*) \quad \text{at} \quad z = 0\,. \tag{3.46}$$

In (3.43)-(3.46), the basic flow u_b has been written in the following form

$$u_b = \hat{U}(z)e^{it} + \hat{U}^*(z)e^{-it}\,, \tag{3.47}$$

where $\hat{U}$ and its complex conjugate $\hat{U}^*$ can be obtained by comparing (3.47) with (3.14) when the exact solution is sought or by comparing it with the approximate solution (3.18).

3.1.6 The morphodynamic response

Once the hydrodynamic response to the bottom perturbations is computed, the temporal development of the amplitude Π of the perturbation can be evaluated from (3.39) and (3.40). It turns out that the temporal development of the bottom can be written as:

$$\frac{d\Pi}{dT} = \Gamma\Pi\,, \quad \Gamma = -\langle 2\delta i\boldsymbol{Q}\rangle\,. \tag{3.48}$$

Here Γ follows from the hydrodynamic response to the bottom perturbations. It turns out that Γ consists of two parts, a real and an imaginary part, $\Gamma = \Gamma_r - i\Gamma_i$, which control the growth and migration of the bottom perturbation, respectively. It turns out that

$$\Pi(T) = \Pi_0 e^{\Gamma T}\,. \tag{3.49}$$

3.2 Numerical model

3.2.1 Hydrodynamics

For the modelling of sand waves in a numerical model, the numerical shallow water model Delft3D-FLOW is used (Lesser et al., 2004). The geometry of the model is similar as the one described in section 3.1.1, the main difference is that the model equations are solved by applying sigma layering in the vertical (Deltaris, 2014), with

$$\sigma = \frac{z - \zeta}{D}\,. \tag{3.50}$$

Here ζ is the free surface elevation and D the total water depth: $H + \zeta$. Here the bed z_b is located at $z = -H_0$ which corresponds to $\sigma = -1$ and the free surface is located at $z = 0$ which corresponds to $\sigma = 0$. In order to capture the initial characteristics of sand waves, the model is run in the 2DV mode, which considers uniformity in the y-direction. In terms of the σ-coordinates, the 2DV hydrostatic shallow water equations are described by

$$\frac{\partial u}{\partial t} + u\frac{\partial u}{\partial x} + \frac{\omega}{(H+\zeta)}\frac{\partial u}{\partial \sigma} = -\frac{1}{g}\frac{\partial \zeta}{\partial x} + \frac{\partial}{\partial x}\left(A_H\left(\frac{\partial u}{\partial x} + \frac{\partial u}{\partial \sigma}\frac{\partial \sigma}{\partial x}\right) + \frac{1}{(H+\zeta)^2}\frac{\partial}{\partial \sigma}\left(A_V\frac{\partial u}{\partial \sigma}\right)\right)\,, \tag{3.51}$$

$$\frac{\partial \omega}{\partial \sigma} = -\frac{\partial \zeta}{\partial t} - \frac{\partial[(H+\zeta)u]}{\partial x}\,. \tag{3.52}$$

Here ω is the vertical velocity, A_H and A_V represent the horizontal and vertical eddy viscosity, respectively. Furthermore, g represent the gravitational acceleration.

In this work the model uses two different turbulence formulations. The first formulation assumes the vertical eddy viscosity A_v to be constant in time and space. The second turbulence formulation, the $k - \varepsilon$ model is a more advanced formulation that calculates both the the turbulent energy k and the dissipation

rate ε. The resulting vertical eddy viscosity is variable in both time and space (for details see Burchard et al. (2008)). The formulations for the vertical eddy viscosity for both closure models are:

$$(1) \quad A_v = \frac{\kappa U H_0 \sqrt{g}}{6C}, \qquad (2) \quad A_v = c_\mu \frac{k^2}{\varepsilon}. \tag{3.53}$$

Here U is the amplitude of the depth averaged flow, κ the von Kármán constant, H_0 the undisturbed water depth, C is the Chézy roughness coefficient and C_μ is a constant calibrated for a local-equilibrium shear layer and set to $C_\mu \approx 0.09$.
At the bed the vertical velocity ω is set to zero and the stress is given by a quadratic friction law, the stress at the free surface is set to zero

$$\tau_b = \rho_w \frac{A_v}{(H+\zeta)} \frac{\partial u}{\partial \sigma} = \rho_w u_* |u_*|, \quad \omega = 0 \quad \text{at} \quad \sigma = -1, \tag{3.54}$$

$$\rho_w \frac{A_v}{(H+\zeta)} \frac{\partial u}{\partial \sigma} = 0, \quad \omega = 0 \quad \text{at} \quad \sigma = 0. \tag{3.55}$$

Here τ_b is the bed shear-stress, ρ_w the water density, which is assumed to be constant, and u_* is the velocity close to the bed

$$u_* = u(\sigma = -1 + \delta). \tag{3.56}$$

The value of δ is located at $\Delta\sigma/2$, i.e. the distance between the middle of the lowest σ-layer to the bed.

3.2.2 Sediment transport

The bed load transport, S_b is calculated with the Meyer-Peter-Muller (Deltaris, 2014), which reads

$$S_b = 8\alpha d_{50} \sqrt{\frac{(\rho_s - \rho_w)}{\rho_w} g d_{50}} \; (\mu\theta - \theta_{\text{crit}})^{3/2}. \tag{3.57}$$

Where d_{50} is the median grain size, α is a calibration coefficient, μ is the ripple factor and θ_{crit} critical Shields parameter (= 0.047). The Shields parameter θ is given by

$$\theta = \left(\frac{u}{C}\right)^2 \frac{\rho_w}{(\rho_s - \rho_w) d_{50}}, \tag{3.58}$$

where the ripple factor reads:

$$\mu = \min\left(\left(\frac{C}{C_{g,90}}\right)^{1.5}, 1.0\right). \tag{3.59}$$

Here C and $C_{g,90}$ are the Chézy coefficient and the Chézy coefficient specifically related to the d_{90} grains size, respectively. Here $C_{g,90}$ is given by

$$C_{g,90} = 18^{10} \log\left(\frac{12(H+\zeta)}{d_{90}}\right). \tag{3.60}$$

Finally, the bed evolution is governed by the sediment continuity equation. This equation simply states that convergence (or divergence) of the bedload transport rate must be accompanied by a rise (or fall) of the bed, which reads

$$(1-p) \frac{\partial z_b}{\partial t} + \frac{\partial S_b}{\partial x} = 0. \tag{3.61}$$

Here z_b is the bed level and $p = 0.4$ is the bed porosity.

4 Material and Methods

In this chapter, a description of the study area will be given (section 4.1) as well as the default model setting (section 4.2) an overview of the experiments conducted to answer the research questions (section 4.3). Finally, section 4.4 describes the methods to analyse the results.

4.1 Study area

In order to address the defined research questions, section 1.5, the environmental parameters of the area of interested have to be examined. The observed sand wave data, grain size and tidal forcing will be discussed.

Selection of location

The area of interest is roughly located at about 52° North and 4°7′ East, which is 20 km off the coast of Katwijk. The study area is a transect between two offshore wind farms, Hollandse Kust Zuid (HKZ) and Hollandse Kust Noord (HKN), Figure 4.1. The transect has an orientation of 70.3 degrees, which is perpendicular to the sand wave crests. The water depth within the research area varies to 30 m Lowest Astronomical Tide (LAT). The seabed consists of sand waves which are superimposed by megaripples. From here onward the study area will be referred to as HKZ.

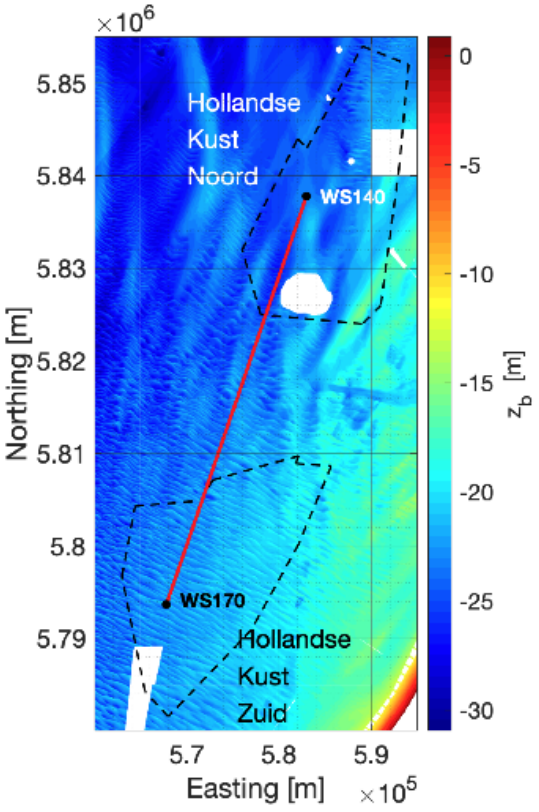

Figure 4.1: General location and bathymetry of the HKZ, data follows from the Dutch Hydrographic service.

Figure 4.2 shows transects of the middle 5 km of the transect of Figure 4.1, which is the area of interest and from heron will be referred to as the HKZ. The bed levels z_b from the transects have an average depth of 23 meters and are constructed with bathymetry data originating from the Hydrographic Office of the Royal Dutch Navy. In Figure 4.2 the black dotted line corresponds to a survey performed on November 15th 1999 and the solid black line to a survey on March 8th 2012. The mean wavelength of the sand wave is defined as the crest-to-crest distance, which is on average 370 m with a standard deviation of 116 m. The mean wave height, which is defined as the crest height-to-trough depth, is on average 1.51 m with a standard deviation of 0.77 m. In the period between the two surveys, the crests have migrated 2.87 m/yr on average (standard deviation of 1.30 m/yr) and the troughs have migrated 1.75 m/yr (standard deviation 1.0 m/yr). An overview of the sand wave data of the HKZ is shown in Table 2.

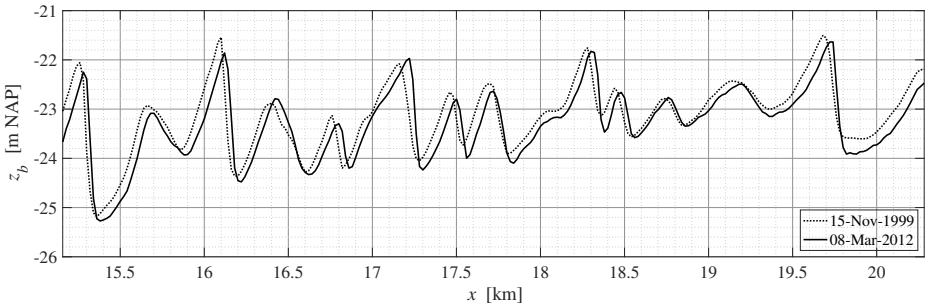

Figure 4.2: Transacts from the HKZ, dotted line corresponds to a survey performed on November 15th 1999 and the solid black line to a survey on March 8th 2012.

Table 2: Overview of sand wave data from the HKZ, data follows from transact done by the Hydrographic Office of the Royal Dutch Navy.

	November 15th 1999	March 8th 2012	Averaged
mean wavelength	368 ± 114 m	372 ± 117 m	370 ± 116 m
mean wave height	1.49 ± 0.76 m	1.53 ± 0.77 m	1.51 ± 0.77 m

Migration of HKZ sand waves	
mean crest migration	2.87 ± 1.30 m/yr
mean trough migration	1.75 ± 1.0 m/yr

The selection of the median grain size from the HKZ follows from a study done by Damen et al. (2018), and is set to be $d_{50} = 0.275$mm. The dominant tidal period is the semi-diurnal tidal constituent, M2 with a depth averaged current amplitude of 0.65 m/s. The period of the M2 tide is 12 hours and 25 minutes.

4.2 Default settings

4.2.1 Linear stability model

The linear stability model calculates the instabilities of perturbations for wave number k, which is related to the wavelength $\lambda = 2\pi/k$. The wave number is scanned ranging from $k = 6.3 \cdot 10^{-3}$ m^{-1} to $k = 3.1 \cdot 10^{-2}$ m^{-1} with 100 steps in wave number space. This range of wave numbers corresponds to a wavelength range of 200 m to 1000 m. The vertical direction is divided into 201 points. The model calculates for 101

points during one tidal cycle (12h25m), which corresponds to a time step dt of 7 minutes and 23 seconds. The model accounts for 16 solutions in the harmonic expansion. The bed slope parameter follows from Besio et al. (2003) and is taken to be $\gamma = 0.05$. The bed slope is related to the angle of repose of sand, via the following relation (Van Rijn, 1993):

$$\gamma = \frac{\theta_{\text{crit}}}{\tan \phi_r}\,, \tag{4.1}$$

here ϕ_r is the angle of repose. With a value for the critical shields parameter of, $\theta_{\text{crit}} = 0.047$ the angle of repose $\phi_r = 43.2°$, via $\tan^{-1}(\theta_{\text{crit}}/\gamma)$. The eddy viscosity and the stress parameter for the default run follow from the newly defined expressions (3.10). Furthermore, the median grain size is 0.275 mm and the sand transport is calculated with the formulation of Meyer-Peter and Müller (1948) , which accounts for both skin friction and form drag. An overview of the default model parameters is given in table 3.

4.2.2 Delft3D-FLOW

The Delft3D-FLOW model is run with a default domain that has a total length L_x of 50 km. In the middle 5 km of the domain ($x = 22.5$ km to $x = 27.5$ km), undulations on the bed are added. The profile of the bed, z_b is given by the following relation

$$z_b = H_0 - \eta A_0 \cos\left(2\pi \frac{x - x_{\text{cen}}}{\lambda_0}\right), \tag{4.2}$$

where H_0 represents the the undisturbed water depth which is 23 m, x_{cen} is the coordinate that lays in the center of the domain (25 km), A_0 the initial amplitude of the undulation in meters and λ_0 the initial wavelength of the undulation. The values for the initial wavelength of the perturbations range from 126 m to 1257 m. In the expression for the bed (4.2) the term η is an envelope function controlling the amplitude in the domain and is defined as follows

$$\begin{aligned}
0 \leq x < 22.5 \text{ km} &: \eta = 0\,, \\
22.5 \leq x < 23.5 \text{ km} &: \eta = \frac{1}{2}\left[1 - \cos\left(\pi\left(x - x_{\text{cen}}\right)\right)\right], \\
23.5 \leq x < 26.5 \text{ km} &: \eta = 1\,, \\
26.5 \leq x < 27.5 \text{ km} &: \eta = \frac{1}{2}\left[1 + \cos\left(\pi\left(x - x_{\text{cen}}\right)\right)\right], \\
27.5 \leq x \leq 50.0 \text{ km} &: \eta = 0\,.
\end{aligned}$$

An example of the initial bed is shown in Figure 4.3. The distribution for η is included in order to allow for a smooth transition of the flat bed to initial perturbations at the center of the domain. The perturbations are relatively far from the boundaries, this to prevent any interaction of the flow with the boundary. In Figure 4.3 the initial undulations have a wavelength of 209 m, the initial amplitude is 0.5% of total water depth, which is 0.115 m.

The models morphodynamics are solved on a staggered grid. At the boundaries the horizontal grid resolution Δx is 500 m, gradually moving to a resolution of Δx is 10 m in the middle of the domain. The vertical domain is divided into 50σ-layers, where the spacing between the layers gradually increase towards the bed. The flow is forced at the lateral boundary and is set to include flow components due to the M2, M4 and M0 tidal constituents. Riemann boundary conditions are imposed at the lateral boundaries. This type of boundary condition allows the tidal waves to cross the open boundary without being reflected back into the computational (van Gerwen et al., 2018; Deltaris, 2014). The Riemann conditions are chosen in such a way that the depth averaged amplitudes and phases of tidal components M2, M4 and M0 in the area of interest (22.5-27.5 km) are equal to the predictions of the DCSM-Zuno v6 model. In the area of interest (Figure 4.1), the depth averaged flow and water levels are extracted from Zuno and the component

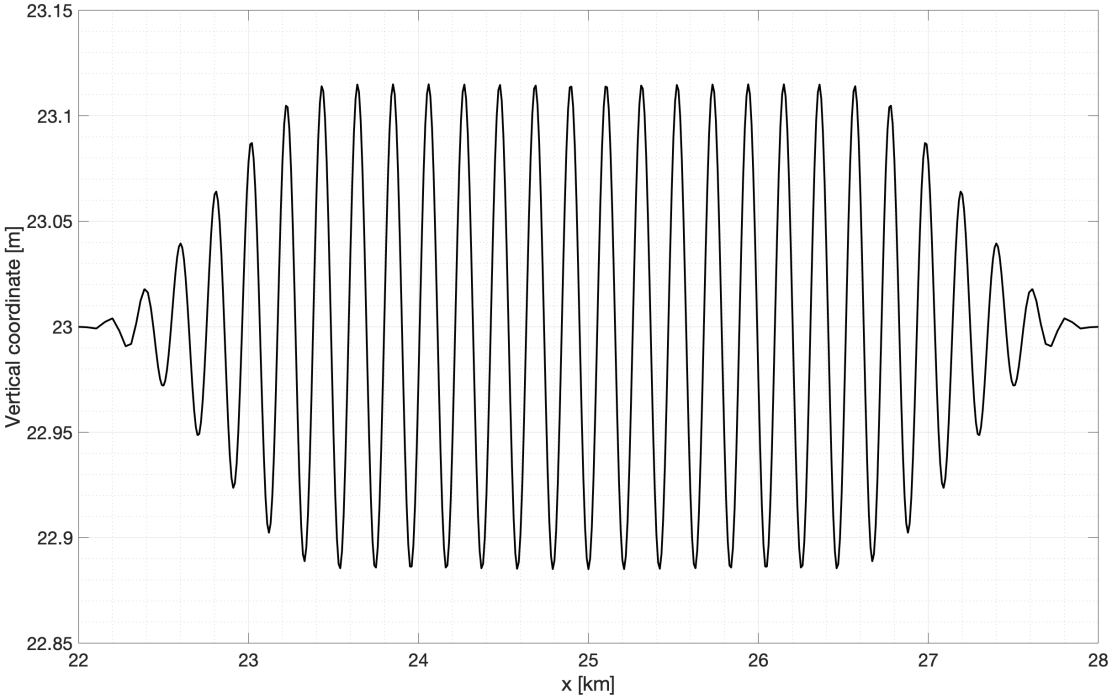

Figure 4.3: Example of initial bed level for sand waves with a wavelength of 209 m, sand wave height is 0.115 m

in the direction of the transect is analysed using T-TIDE (for details see Pawlowicz et al. (2002)). The results for the amplitude and the phase of the tidal constituents including the residual current are listed in Table 3.
Furthermore, the bed slope parameter $\alpha_{bs} = 3$, corresponding to an angle of repose of $\phi_r = \tan^{-1}(1/\alpha_{bs}) = 18.5°$. The model is run with a constant eddy viscosity in the horizontal and vertical direction A_H and A_V. The values are chosen such that it corresponds to the values in the linear stability model, where $A_H = A_V = 0.053\,\mathrm{m^2 s^{-1}}$. The median grain size is 0.275 mm and the sand transport is calculated with the formulation of Meyer-Peter and Müller (1948). A spin-up interval of 2 days is added, allowing the flow to adjust to the bed before any morphological changes are permitted. After the spin-up the model is run for a total of 5 days. An overview of the default model settings is shown in table 3.
The relative phase shift between the M4 and M2 tidal constituent is given by the following relation

$$\phi_{M4-M2} = \phi_{M4} - 2 \cdot \phi_{M2}\,, \tag{4.3}$$

where ϕ_{M2} and ϕ_{M4} represents the phases of the M2 and M4 tidal constituents respectively.

Table 3: Overview of default model settings for the linear stability model and the Delft3D-FLOW model.

Overview of default model parameters		
Parameter	Value	Description
Hydrodynamics		
H	23 m	Water depth
U_{M2}	0.65 m s^{-1}, 85°	Amplitude and phase M2 current
U_{M4}	0.04 m s^{-1}, 134°	Amplitude and phase M4 current
U_{M0}	0.004 m s^{-1}	Amplitude residual current
ϕ_{M4-M2}	−36°	Relative phase shift between M4 and M2
σ	$1.4 \cdot 10^{-4}$ s^{-1}	Angular frequency M2 tide
Morphodynamics		
Δ_r	$3.4 \cdot 10^{-2}$m	Typical height of ripples
l	0.2m	Typical length of ripples
Δ_{mr}	0.2m	Typical height of mega ripples
l_{mr}	10m	Typical length of mega ripples
ρ_s	2650 kg m^3	Sediment density
ρ	1024 kg m^3	Water density
d_{50}	0.275 mm	Median sand grain size
p	0.4	Porosity of bed
Specific linear stability model parameters		
$\mathcal{N}$	16	Number of solutions in the harmonic expansion
k	$6.3 \cdot 10^{-3}$ - $3.1 \cdot 10^{-2}$ m^{-1}	Range of scanned wave number
dk	100	Number of steps in wave number space
dz	201	Number of steps in vertical domain
dt	101	Number of steps in tidal period
$U_{M0}U_{M2}$	$6.15 \cdot 10^{-3}$ m/s	Amplitude ratio of M0/M2
$U_{M4}U_{M2}$	$6.15 \cdot 10^{-2}$ m/s	Amplitude ratio of M4/M2
γ	0.05	Bed slope (dimensionless)
Specific Delft3D-FLOW model parameters		
L_x	50 km	Length of domain
Δx	10 m	Horizontal grid spacing at the area of interest
σ	50	Steps in vertical direction
dt	6 s	Hydrodynamic time step
A_H	0.053 m^{2}s^{-1}	Horizontal eddy viscosity
A_V	0.053 m^{2}s^{-1}	Vertical eddy viscosity
λ_0	126-1257 m	Range of initial sand wave wavelength
A_0	0.115 m	Initial sand wave amplitude
α_{bs}	3	Bed slope parameter

4.3 Experiments

Linear stability model

To answer the research questions, several experiments were conducted. First the effect of the newly defined closure relation on the basic flow, the hydrodynamics and sand wave characteristics was investigated with the linear stability model. This was done by running the model for the default settings described in section 4.2.1. The model incorporates the newly defined closure relation (3.10) and the closure relation described by Hulscher and van den Brink (3.8).
Next, the impact of the bed shear-stress incorporated by the sediment transport formula on sand wave characteristics was investigated. This was done by changing the expression for the bed shear-stress included in the sediment transport formula. The bed shear-stress is changed from the total bed shear-stress (skin friction and form drag) in the default case to only including the skin friction, see section 2.1.3
The sensitivity of environmental parameters to sand wave characteristics was investigated with the linear stability model for the default case. Here the following environmental parameters and their range are investigated; the water depth H is varied between 15 and 30 m, the grain size d_{50} is varied between 0.15 and 0.40 mm, the amplitude ratio of M4/M2, U_{M4}/U_{M2} is varied between 0 and 0.2, the relative phase shift between M4 and M2, ϕ_{M4-M2} is varied between -180 and 180°. Finally, the amplitude ratio of M0/M2, U_{M0}/U_{M2} is varied between 0 and 0.02 the An overview of the conducted experiments is given in table 4.

Delft3D-FLOW

Finally, in order to be able to make a comparison of the results obtained with the linear stability model with a numerical model, sand waves characteristics were investigated with Delft3D-FLOW model. The initial growth and migration rates of sand waves were investigated for the two different models for turbulence in the Delft3D-FLOW model. First, sand wave characteristics with a constant eddy viscosity for the following initial sand wavelengths were investigated: [126 m, 140 m, 157 m, 180 m, 209 m, 251 m, 314 m, 419 m, 628 m, 1257 m]. Next, the same runs were done with the k-ϵ turbulence model. An overview of the conducted experiments is given in table 4.

Table 4: Overview of conducted experiments, here the abbreviation LSM means linear stability model and D3D is the Delft3D-FLOW model.

Experiment	Description
1A	LSM: Default case new formulation for closure relation
1B	LSM: Default case closure relation described by Hulscher and van den Brink (2001)
1C	D3D: Default case constant eddy viscosity model
1D	D3D: Default case k-ε turbulence model
2A	LSM: Skin friction only
3A	LSM: Varying water depth
3B	LSM: Varying grain size
3C	LSM: Varying amplitude ratio of M4/M2
3D	LSM: Varying amplitude ratio of M0/M2
3E	LSM: Varying phase shift between M4 and M2

4.4 Analysis of model results

Linear stability model

Section 2.3 explains how the temporal development of the bottom amplitude Π (3.49) leads to quantities for the growth and migration. It also discussed that the values for Γ_r and Γ_i, which control the amplification/decay and the migration, respectively, are calculated for the scanned wave number range k. In order to analyses the computed sand wave characteristics, the fast growing mode is determined. The wavelength of the sand waves $\lambda = 2\pi/k_{\text{fgm}}$, the migration speed $\Gamma_i(k_{\text{fgm}})$ and the e-folding time $1/\Gamma_r(k_{\text{fgm}})$ all follow from the fast growing mode.

Delft3D-FLOW model

The initial growth and migration in the Delft3D-FLOW model were determined using linear stability analysis. In this analyses the bed level z_b consists of a basic state z_{b0} with small perturbations, h, superimposed on the bed. The perturbations are small relative to the basic state of the bed (Besio et al. (2008); Krabbendam (2018))

$$z_b(x,t) = z_{b0}(x) + h(x,t) \qquad \text{with } |h| \ll |z_{b0}| \tag{4.4}$$

Linearisation of the problem is allowed because the assumption is made that the perturbations are small, yielding the following expression for the small perturbations h,

$$\frac{\partial h(x,t)}{\partial t} = \Gamma(t)h(x,t) \tag{4.5}$$

Here Γ is a complex expression consisting of a real and imaginary part: $\Gamma(t) = \gamma_r(t) + i\gamma_i(t)$. The value for this complex expression depends on the initial perturbation, the sand characteristics and on the flow. Due to the oscillatory character of the tide, the periodic function in time, Γ, can be split into a time average value $\bar{\gamma}$ and a periodic part $\tilde{\gamma}$. The solution of the equation for the development of the initial perturbations (4.5) is

$$h(x,t) = A_0(x)\exp\left[\int_0^t \Gamma(t)\mathrm{d}t\right] \tag{4.6}$$

Where $A_0(x)$ denotes the initial amplitude of the bottom perturbation. This solution can be plugged into the first expression for the bed (4.4), resulting in the following expression for the bed evolution

$$z_b(x,t) = z_{b0}(x) + A_0(x)/2\exp\left[\bar{\gamma}_r t + \int_0^t \tilde{\gamma}_r(t)\mathrm{d}t\right]\exp\left[i\left(k_x x + \bar{\gamma}_i t + \int_0^t \tilde{\gamma}_i(t)\mathrm{d}t\right)\right] + c.c.. \tag{4.7}$$

Eq. (4.7) describes a spatial periodic bottom perturbation where the wavelength λ depends on the wave number k_x since $\lambda = 2\pi/k_x$. Moreover, the growth/decay of the perturbation is by the time-averaged value $\bar{\gamma}_r$ of Γ_r. The migration is controlled by the time-averaged value of $\bar{\gamma}_i$ of Γ_i, where the phase speed is $c_x = -\bar{\gamma}_i/k_x$. The periodic parts of the growth and migration rate ($\tilde{\gamma}_r$ and $\tilde{\gamma}_i$) describe the oscillation of the profile during a tidal cycle. These oscillations are characterised by a very small amplitude, and there for these terms can be neglected, yielding for the bottom perturbation

$$h(x,t) = A_0\exp\left[\bar{\gamma}_r t + i\left(k_x x + \bar{\gamma}_i t\right)\right] \tag{4.8}$$

If $\bar{\gamma}_r > 0$ ($\bar{\gamma}_r < 0$), the bottom perturbation is unstable and grows (decays) exponentially in time. The perturbation is stable when $\bar{\gamma}_r = 0$.
For convenience the time-averaged parts of the initial growth and migration rates will denoted by γ_r and

γ_i, respectively. Since the perturbations of the bed are periodic, the perturbation h can be expressed as a Fourier series A_n

$$A_n\left(k_n, t\right) = \sum_{j=0}^{N_x-1} h\left(x_j, t\right) \exp\left(i k_n x_j\right) \ . \tag{4.9}$$

Where, $x_j = j\Delta x$ with $j = 0, 1, 2, ..., (N_x - 1)$ and the wave number

$$k_n = \frac{2\pi n}{N_x}, \quad \text{with } n = -\frac{N_x - 1}{2}, .. \frac{N_x - 1}{2} \ . \tag{4.10}$$

The inversion of the Fourier series is,

$$h\left(x_j, t\right) = \sum_{n=-\frac{N_x-1}{2}}^{\frac{N_x-1}{2}} A_n\left(k_n, t\right) \exp\left(i k_n x_j\right) \tag{4.11}$$

Combining the expression for the bed perturbation (4.8) with (4.11) and taking the natural logarithm, yield the following equations for the growth- and migration rates

$$\Gamma_r = \frac{1}{T_{01}} \Re \left\{ \ln\left(\frac{A_0}{A_1}\right) \right\} \ , \tag{4.12}$$

$$\Gamma_i = -\frac{1}{k_x T_{01}} \Im \left\{ \ln\left(\frac{A_0}{A_1}\right) \right\} \ . \tag{4.13}$$

Where, $T_{01} = t_1 - t_0$ and t_1, t_0 being the initial time and the time for with $A = A_1$, respectively.

5 Results

This chapter is divided into two sections. Section 5.1 shows the results of the linear stability model, Section 5.2 shows the results of the numerical model. Section 5.1 starts with presenting the initial flow of the model. Followed by the results of the growth and migration for the two different closure relations, the residual flow and the influence of form drag in the transport formulation. Finally, section 5.1 shows the sensitivity of sand wave characteristics on environmental parameters.
In Section 5.2 the initial flow is shown first, these are shown for the two different viscosity models. Secondly, the growth rates and migration for these models are shown for different initial perturbations along with the residual circulation.

5.1 Linear stability model

The model configuration and the default parameter settings have been presented in Section 4.2.1. The default runs employ two different closure relations, for details see Section 3.1.2. The different closure relations have an impacted on the stress and the eddy viscosity. It turns out that, for the closure relation described Hulscher and van den Brink (2001) (HB01 hereinafter) $A = 0.0523$ m^{2}s^{-1} and $\tilde{s} = 0.0434$ m^{-1}, where for the new formulation the eddy viscosity and stress are, $A = 0.0185$ m^{2}s^{-1} and $\tilde{s} = 0.1153$ m^{-1}.

5.1.1 The flow

Basic flow

Figure 5.1 shows a contour-color plot of the basic flow as function of the scaled distance to the bottom (in units of water depth) and the scaled time (in units of the tidal period) of the linear stability model for the two different closure relations. Here figure 5.1 (a) shows the result for the new formulation while figure (b) shows the result for the closure relation described by HB01. It can be seen that the new formulation experiences an enhanced shear in the flow, whilst it attains higher maximum flow velocity compared with figure (b). For the closure relation described by HB01 the flow at the bottom is higher. For both cases the maximum positive basic flow is stronger than their negative flow values, revealing asymmetry in the flow.

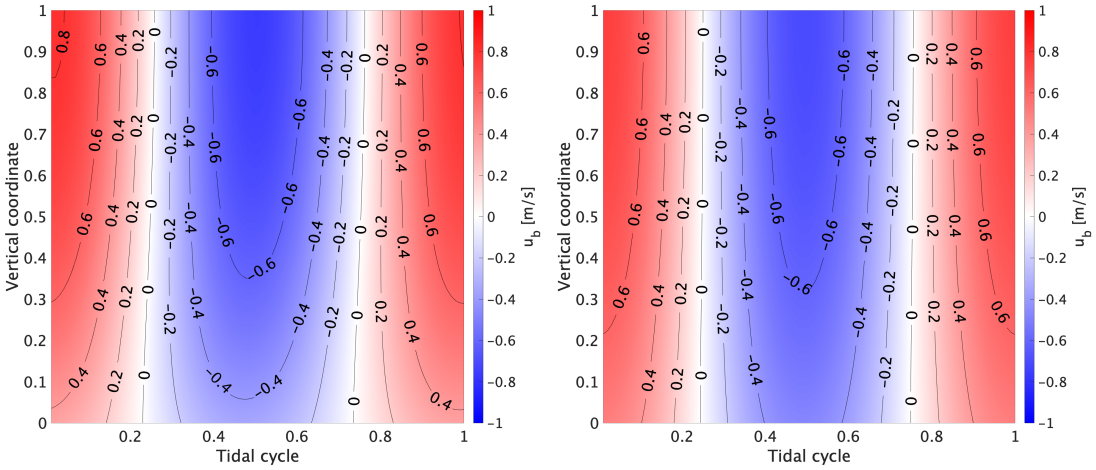

(a) New formulation **(b)** HB01

Figure 5.1: Contour-color plot of the basic flow as function of the scaled distance to the bottom (in units of water depth) and the scaled time (in units of the tidal period).

Tidal constituents of the basic flow

Figure 5.2 shows the velocities for the same phase of the tidal cycle as function of the water depth due the residual M0 (a), the semi-diurnal lunar tide M2 (b) and its first overtide M4 (c). The newly defined closure relation is indicated with a solid line, the relation of HB01 with a dotted line. It can be seen that the new formulation attains a lower velocity compared to HB01 formulation at the bed ($z = 0$) for all three tidal constituents. All the velocities for the new formulation reach higher values compared to HB01 formulation higher up the water column. This is expected from Figure 5.1, which shows similar behaviour for the basic velocity. Furthermore, it can be seen that the largest contribution to the basic flow comes from the semi-diurnal lunar tide M2 tide.

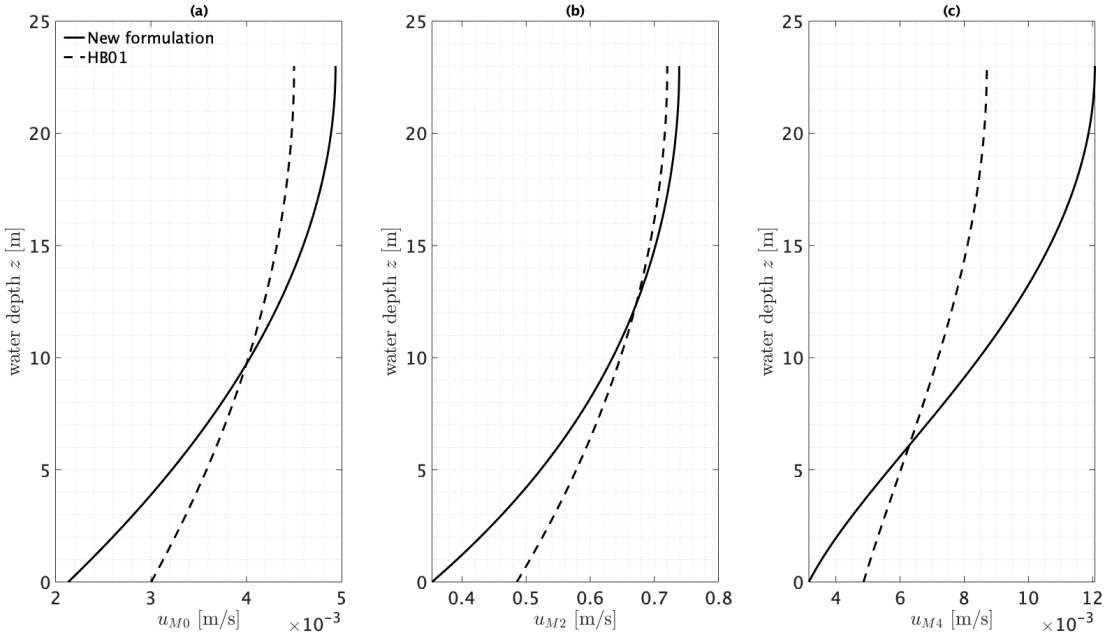

Figure 5.2: Velocity in m/s of the basic flow as function of the water depth due the residual M0 (a), the semi-diurnal lunar tide M2 (b) and its first overtide M4 (c). Closure relation are indicated with a solid line for the new formulation and a dotted line for HB01.

5.1.2 Results of the nominal case

Figure 5.3 presents the results for the growth rate (a) and migration speed (b) for different closure relations. Here the newly formed closure relation is depicted by the dotted lines whilst the formulation of HB01 is depicted by the solid line. In Figure 5.3 (a), it can be seen that the growth rates attain higher values for increasing wave numbers k, followed by a decrease in growth rates. This indicates that there is a maximum, the fastest growing mode. The fastest growing mode for both closure relations are indicated with grey lines. It can be seen that the fastest growing mode for the new formulation is shifted to a large k value, leading to a smaller sand wavelength. Corresponding values for the new formulation are: $k = 1.44{\cdot}10^{-1}$ m^{-1}; $\lambda = 435$ m. For the formulation of HB01 these values are: $k = 9.1 \cdot 10^{-2}$ m^{-1}; $\lambda = 690$ m. The growth rate increases from 0.0217 yr^{-1} to 0.0445 yr^{-1} for the new formulation, leading to a decrease of the e-folding time. The e-folding times for the new formulation and the formulation of HB01 are 22.5 yr and 46.0 yr, respectively. The model computes of the fastest growing mode larger migration rate for

the new formulation of c_m = 1.61 m/yr. For the formulation of HB01 the model computes of the fastest growing mode a migration rate of c_m = 1.29 m/yr. The results obtained with the new formulation of the closure relations agree more with the observed sand waves at the HKZ. At the HKZ the sand waves have an average wavelength of 371 ± 117 m and an average migration speed of 2.31 ± 1.15 m/yr.

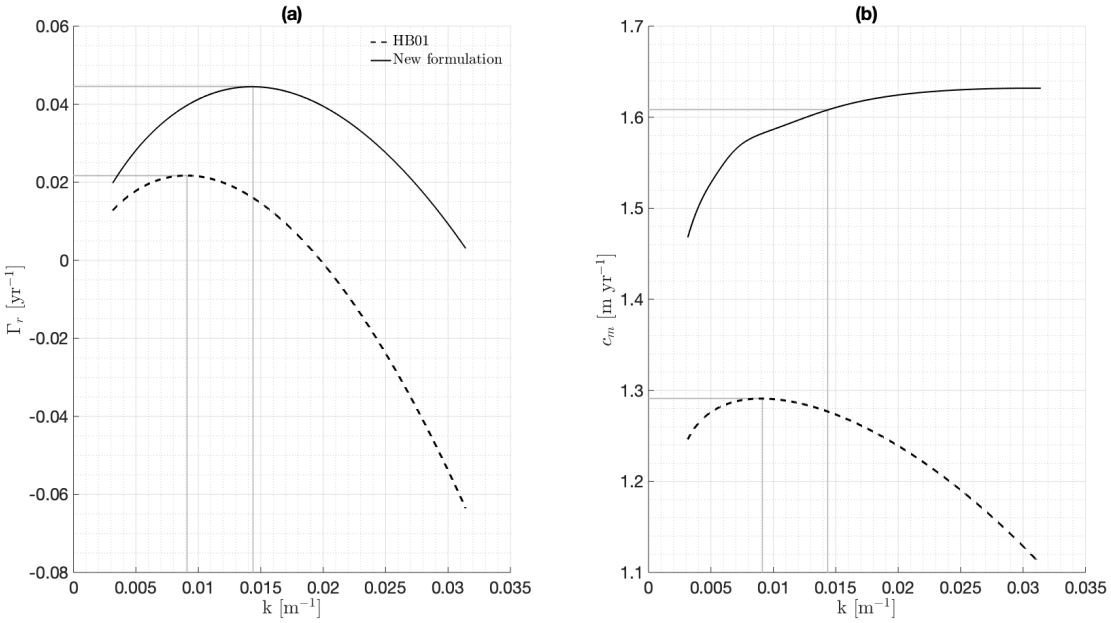

Figure 5.3: Influence of the closure relations employed in the model on the generation and migration of sand waves. Here (a) shows the growth rate Γ_r as a function of the wave number k of the bottom perturbation and (b) migration speed c_m as function of the wave number k. It can be seen that the preferred wave number (vertical lines) increases for the new formulated closure relation from: $k = 9.1 \cdot 10^{-2}\text{m}^{-1}$ to $k = 1.44 \cdot 10^{-1}\text{m}^{-1}$.

Residual circulation

The effect of the sediment transport, induced by the steady recirculating cells, originates from the interaction of the basic flow with bottom perturbations. These residual recirculating cells, which are tidally averaged, are shown for both closure relations in Figure 5.4. Figure 5.4 (a) shows the residual cells for the new formulation and figure (b) shows the residual cells for the closure relation of HB01. Here, contour plots are shown for the non-dimensional stream function as a function of height and the bottom perturbations in the kx-domain. The bottom perturbations follow from the preferred wavelength, which are taken for the new formulation and the one of HB01, λ = 435m and λ = 690m, respectively. Here, the applied initial bottom perturbation is $\Pi_0 = \cos(\text{k}x)$, leading to crests of the perturbation located at 0, 2π and 4π. In the lower part of the cells, the flow is directed towards the crests. The residual circulation is weaker for the new formulation, this is due to the weaker flow in the basic state. The increased stress for the new formulation lowers the center of the residual circulation cell, the center is located at $z/H = 0.28$ for the new formulation instead of $z/H = 0.36$ for the closure relation of HB01.

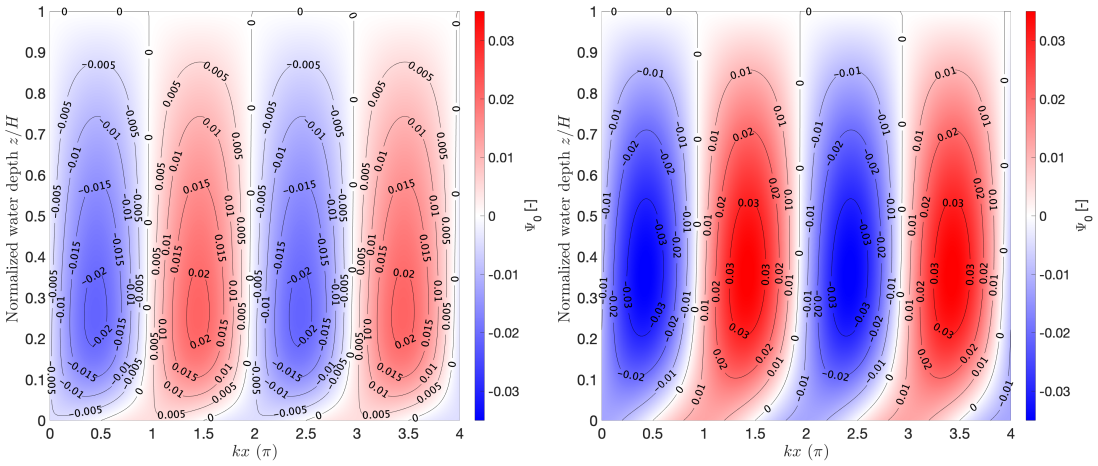

(a) New formulation **(b)** HB01

Figure 5.4: Contour plot of the non-dimensional residual stream function Ψ_0 for (a) the new formulations of the closure relation and (b) the closure relation described by Hulscher and van den Brink (2001). The figure shows perturbations in the kx-domain, with crests located at 0, 2π and 4π. The vertical coordinate is scaled with the undisturbed water depth.

5.1.3 Influence of form drag

In the results shown in Section 5.1.2 the sediment transport was calculated with the formulation by Meyer-Peter and Müller (1948), which uses the total bed shear stress, similar to Besio et al. (2003). However, in Section 2.1.3 it is explained that only skin friction, which is part of the total bottom shear-stress, contributes to sediment transport. The allowance of the form drag into the bottom roughness, which is incorporated by the sediment transport formula is investigated.

Figure 5.5 shows the result of a model run without allowing form drag into the sediment transport formula. Here, only the newly defined closure relation is investigated. It can be seen, in Figure 5.5 (a), that the growth rates attain higher values for increasing wave numbers k, followed by a decrease in growth rates. This indicates the presence of a fastest growing mode, which is located at $k_{\text{fgm}} = 7.3 \cdot 10^{-2}$ m^{-1}. This corresponds to a sand wavelength of $\lambda = 880$ m, a growth rate of $\Gamma_r = 2.5 \cdot 10^{-3}$ yr^{-1} and an e-folding time of 405 yr. The wavelength and e-folding time are significantly larger than the nominal model run (wavelength nominal case: $\lambda = 435$ m, e-folding time: 22.5 yr). The model thus computes a larger wavelength when it only allows for skin friction into the sediment transport. Figure 5.5 (b) shows the preferred migration speed. It turns out that computed the migration speed is $c_m = 0.64$ m yr^{-1}, this is a lower migration compared to the nominal case (migration nominal case: $c_m = 1.61$ m/yr).

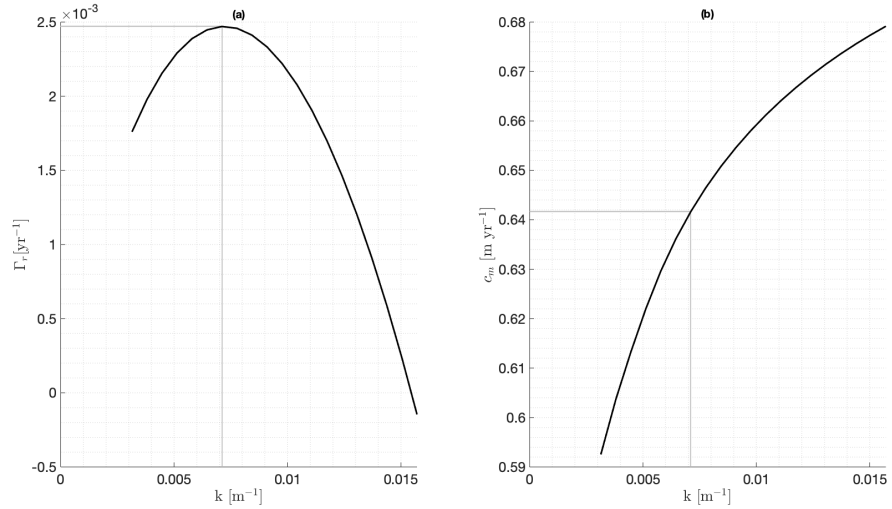

Figure 5.5: Model run without allowing form drag into the sediment transport formula. The model is run with the default settings for the new formulation of the closure relations, showing the growth rate (a) and the migration speed (b). The selection of the fast growing mode and the corresponding growth- and migration rates are indicated by the gray line. It turns out that the preferred wave number is at $k_{\text{fgm}} = 7.3 \cdot 10^{-2}$ m^{-1} corresponding to $\Gamma_r = 2.5 \cdot 10^{-3} y^{-1}$. The preferred migration speed is $c_m = 0.64$m yr^{-1}.

5.1.4 Sensitivity to environmental parameters

The linear stability model is employed to investigate the wavelength, migration, and e-folding time of tidal sand waves and five environmental parameters: median grain size, water depth, tidal current amplitude ratio M0/M2, tidal current amplitude ratio M4/M2, and the relative phase difference between M4 and M2. The model is run with the default parameters, while allowing for changes in the investigated environmental parameter. The range of the environmental parameters are listed in Section 4.3. The model computes the fastest growing mode and the corresponding growth- and migration rates for the environmental parameters. These are subsequently added in contour plot and the results are shown in figures 5.6 to 5.11, where the dotted lines indicate the HKZ environmental values.

Influence of the water depth and median grain size on sand wave characteristics

The dependence of sand wavelengths on the water depth and grain size is shown in figure 5.6. The model results indicate that increasing depths result in longer sand waves. In the same figure, the dependence of the sand wavelength on the median grain size is shown. The model computes increasing wavelengths for coarser median grain size. Large (short) sand waves are computed for the large (shallow) water depths with coarse (fine) sand grains. The biggest computed sand wavelength is $\lambda = 810$ m, the shortest sand wave attains a wavelength of $\lambda = 135$ m.

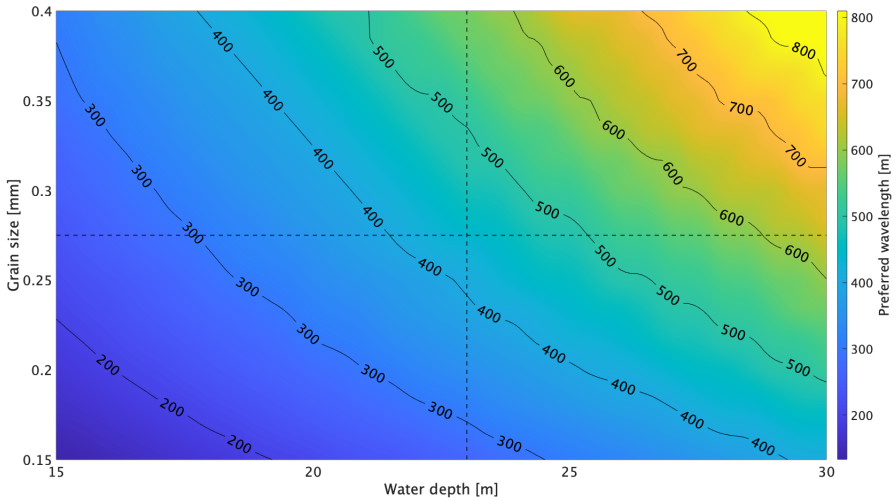

Figure 5.6: Contour plot showing the dependence of the preferred wavelength of the sand waves on the water depth (horizontal axis) and grain size (vertical axis). The gray dotted lines indicate the default values. Blue indicates shorter preferred wavelengths while yellow colors indicate larger wavelengths.

Figure 5.7 shows the dependence of the migration speed on the water depth and grain size. The figure shows that for an increasing water depth the sand waves migrate at slower rates. The model computes migration rates of 2.8 m yr^{-1} for a depth of 15 m, decreasing to 1.3 m yr^{-1} for depths approaching 30 m. It can be seen that for depths around 10 m the influence of the grain size on sand wave migration is weak. The influence of the grain size becomes more apparent for larger water depths, where it can be seen that sand waves migrate faster for increasing grain size.

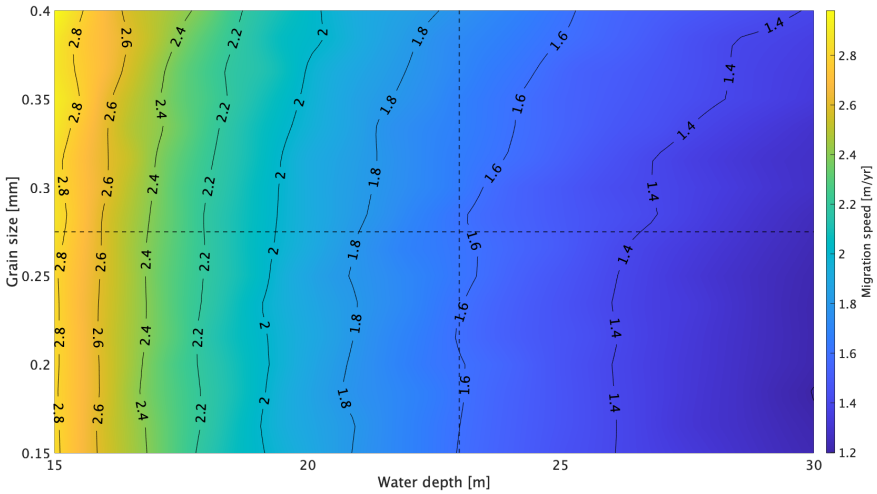

Figure 5.7: Contour plot showing the dependence of the migration speed of the preferred sand wave on the water depth (horizontal axis) and grain size (vertical axis). The gray dotted lines indicate the default values. Blue colors indicate slower migrating sand waves while yellow colors indicate faster migrating sand waves.

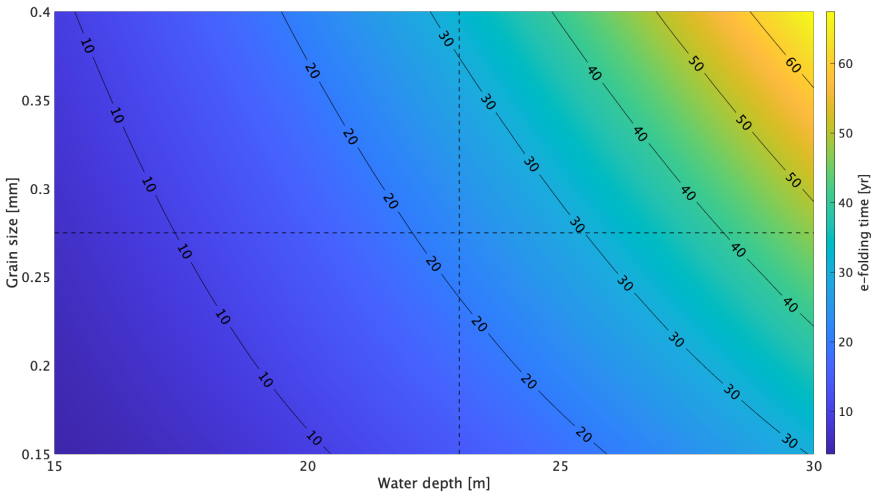

Figure 5.8: Contour plot which shows the dependence of the *e*-folding time on the water depth (horizontal axis) and grain size (vertical axis). The gray dotted lines show the values for the default values. Blue colors indicate shorter *e*-folding times while yellow colors indicate longer *e*-folding times.

The response of the *e*-folding time of the sand waves on the varying water depth and grain size is shown in Figure 5.8. The model results indicate that increasing depths result in larger *e*-folding times. In the same figure, the dependence of the sand wavelength on the median grain size is shown. The model computes increasing *e*-folding time for coarser median grain size. Longer (shorter) *e*-folding time are computed for the large (shallow) water depths with coarse (fine) sand grains. The largest computed *e*-folding time is 66 yr, the shortest computed *e*-folding time is 4 yr.

Influence of tidal current amplitude ratio (M4/M2) and the relative phase difference on sand wave formation

The dependence of sand wave formation and migration on the tidal current amplitude ratio of M4/M2 and their relative phase difference is show in Figures 5.9-5.11. Note that the model inputs are both the current ratio of M0/M2 and M4/M2. Only the amplitude ratio of M4/M2 is varied, meaning that the model results should be interpreted as a change in M4 tidal current only, since the M2 is kept constant.

The model findings for the sand wavelengths are shown in Figure 5.9. Here it can be seen that some non-linear effects are present as the dependency of the wavelength peaks for certain phase differences. When the model computes for 0° or 180° phase difference then the effect of the current amplitude ratio of M4/M2 is weak. For a phase difference of 0° and 180° the wavelength ranges from 435 m to 445 m. Furthermore, it appears that the maximum influence of the current amplitudes is located at a phase difference of -65° and 115°. Here, the influence of the tidal current amplitude ratio is stronger. The model computes the largest dependency in the current ratios for a relative phase difference of 115°, where the wavelengths range from to 435 m to 480 m. For the current ratio M4/M2, the model computes a constant wavelength of 435 m when the ratio is 0, since the model does not allow for M4 currents and thus computes no wavelength dependency on their phase difference. The largest wavelengths are found at the largest current ratios.

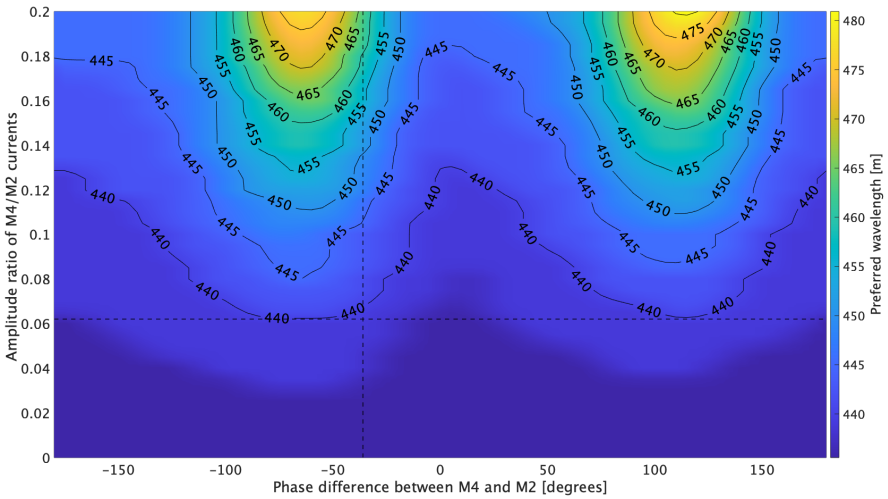

Figure 5.9: Contour plot which shows the dependence of the sand wavelength on the relative phase difference: $\phi_{M4-M2} = \phi_{M4} - 2 \cdot \phi_{M2}$, where ϕ the phase of the depth averaged current on the horizontal axis and tidal current amplitude ratio of M4/M2 on the vertical axis. The gray dotted lines show the default values. Blue colors indicate shorter sand waves while yellow colors indicate longer sand wavelengths.

The dependence on the migration speed of the preferred sand wavelength is shown in Figure 5.10. In the figure the blue color indicates negative values for the migration speed, meaning that the sand waves migrate in the direction opposite of the residual current. Greenish/yellow color indicates positive values for the migration and thus a direction of migration with the residual current. The largest migration speeds are observed for phase differences of 25° and -155° in combination with the largest amplitude ratio.

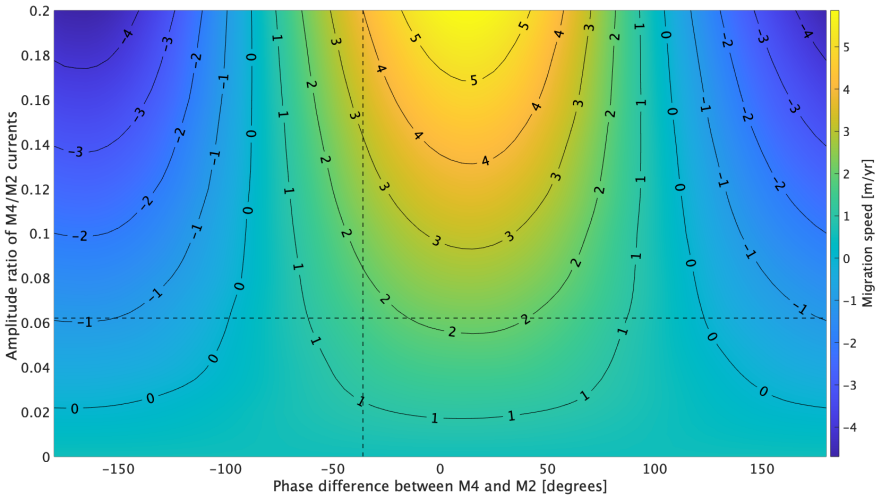

Figure 5.10: Contour plot which shows the dependence of the sand wave migration rates on the relative phase difference between M2 and M4 (horizontal axis) and tidal current amplitude ratio of M4/M2 (vertical axis). The gray dotted lines show the default values. Blue (yellow) colors indicate migration against (with) the residual current.

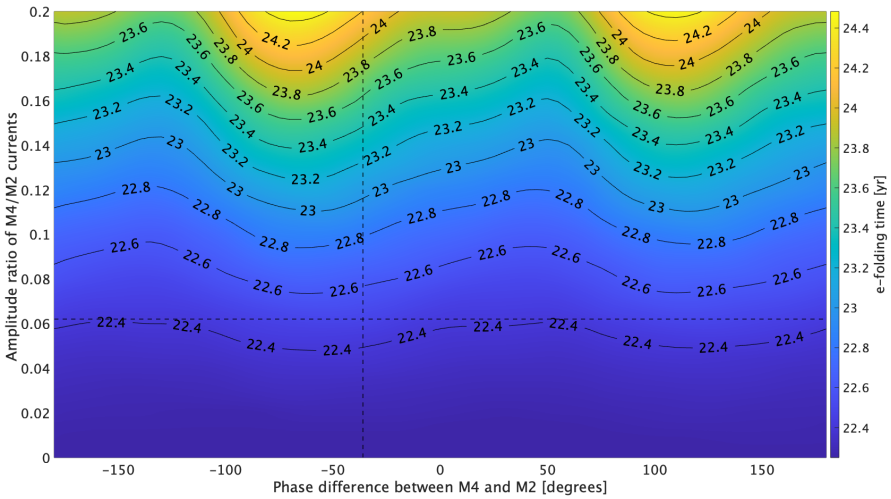

Figure 5.11: Contour plot which shows the dependence of the *e*-folding time of sand waves on the relative phase difference between M2 and M4 (horizontal axis) and tidal current amplitude ratio of M4/M2 (vertical axis). The gray dotted lines show the default values. Blue colors indicate shorter *e*-folding times while yellow colors indicate longer *e*-folding times.

Figure 5.11 shows the *e*-folding time of the preferred sand waves on the tidal current amplitude ratio of M4/M2 and their relative phase difference. The model computes maximums for the *e*-folding time at the largest current amplitude ratio and at a phase difference of -65° and 115°, where the *e*-folding time is 24.3 yr. Furthermore, the influence of the amplitude ratio is relatively weak. However, largest *e*-folding time is computed for the largest amplitude ratio. The influence of the phase difference is more apparent with a maximum range of 22.3 yr to 24.3 yr at 115°.

Influence of tidal current amplitude ratio (M0/M2) and the water depth on sand wave formation

The dependence of sand wave formation and migration on the tidal current amplitude ratio of M0/M2 and their relative phase difference is show in Figures 5.12-5.14. Note that the model inputs are both the current ratio of M0/M2 and M4/M2. Only the amplitude ratio of M0/M2 is varied, meaning that the model results should be interpreted as a change in M0 tidal current solely since the M2 is kept constant.

The model findings for the sand wavelengths are shown in Figure 5.12. Here it can be seen that preferred wavelength of the sand waves does not depend on the current amplitude ratio of M0/M2. The largest (shortest) wavelengths are indicated with yellow (blue) and observed at the deepest (shallowest) water depths. Furthermore, it can be seen that the largest computed wavelength is 625 m and the shortest computed wavelength is 235 m.

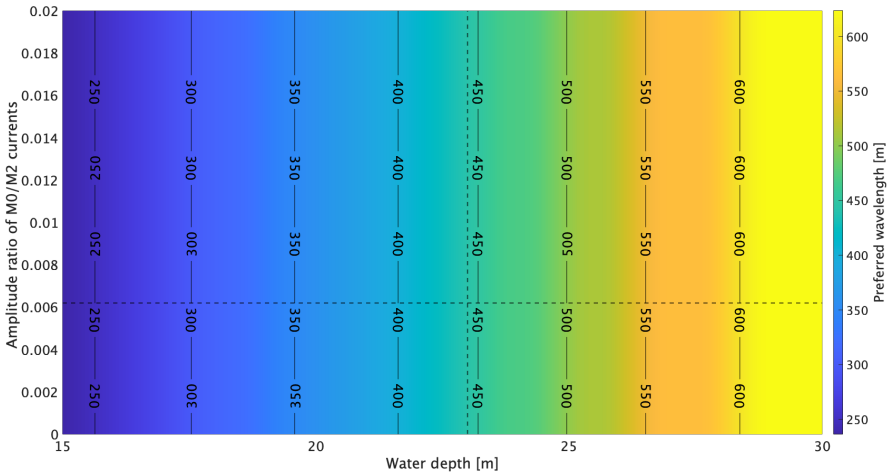

Figure 5.12: Contour plot which shows the dependence of the preferred wavelength of the sand waves on the water depth (horizontal axis) and tidal current amplitude ratio of M0/M2 (vertical axis). The gray dotted lines show the values for the default values. Blue colors indicate shorter preferred wavelengths while yellow colors indicate larger wavelengths.

Figure 5.13 shows the dependence of the migration speed on the water depth and the tidal current amplitude ratio of M0/M2. The figure shows that for an increasing water depth the sand waves migrate at slower rates. Furthermore, it can be seen that for an increase tidal current amplitude ratio of M0/M2 that the sand waves will migrate faster. The model computes the fastest migration speed of 5.25 m yr^{-1} for the shallowest water depth with the largest amplitude ratio. The slowest migration speed is 0.9 m yr^{-1} for the deepest water depth with the smallest amplitude ratio.

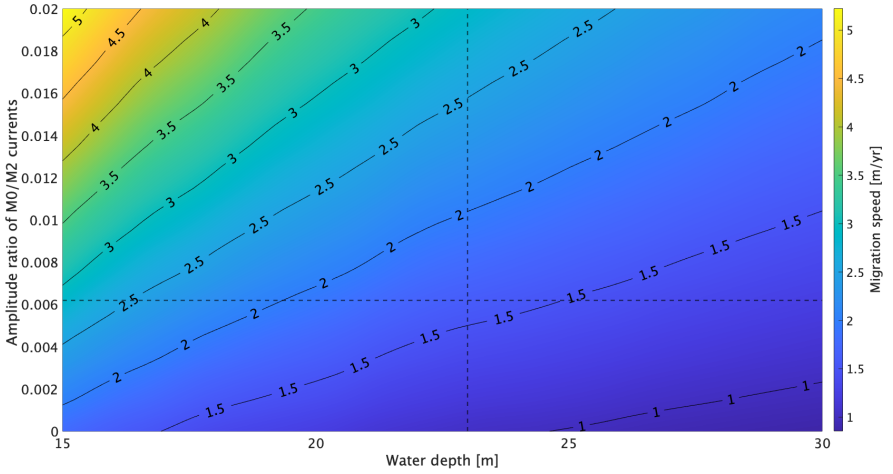

Figure 5.13: Contour plot which shows the dependence of the migration speed of the preferred sand waves on the water depth (horizontal axis) and tidal current amplitude ratio of M0/M2 (vertical axis). The gray dotted lines show the values for the default values. Blue colors indicate slower migrating sand waves while yellow colors indicate faster migrating sand waves.

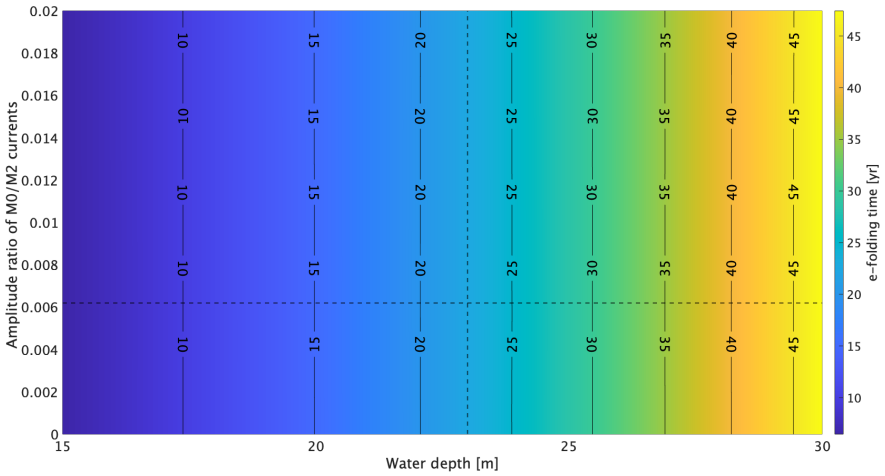

Figure 5.14: Contour plot which shows the dependence of the e-folding time of sand waves on the water depth (horizontal axis) and tidal current amplitude ratio of M0/M2 (vertical axis). The gray dotted lines show the values for the default values. Blue colors indicate shorter e-folding times while yellow colors indicate longer e-folding time.

The response of the e-folding time of the sand waves on the varying water depth and tidal current amplitude ratio of M0/M2 is shown in Figure 5.14. Here it can be seen that the e-folding time of the sand waves do not depend on the current amplitude ratio of M0/M2. The longest (shortest) e-folding time are indicated with yellow (blue) and observed at the deepest (shallowest) water depths. Furthermore, it can be seen that the longest computed e-folding time is 47 yr and the shortest computed e-folding time is 8.4 yr.

5.2 Numerical model

This sections shows the results obtained with the numerical model Delft3D-FLOW. The main difference, compared to the linear stability model is that the numerical model uses the shallow water equations. This model thus assumes that the horizontal length scale is much greater than the vertical length scale. Furthermore, the model uses a more realistic turbulence formulation. However, more refined turbulence models come at the cost of more computational effort. The model configuration and the default parameter settings have been presented in Section 4.2.2. The default runs employ two different eddy viscosity formulations, for details see Section 3.2.1. In this section, the initial state of the flow is shown first. Secondly, the growth rates and migration for different initial perturbations is shown along with the residual circulations.

5.2.1 Response of the flow

Basic flow

Figure 5.15 shows the basic flow of the numerical model for the two different eddy viscosity formulations. Here figure 5.15 (a) shows the result for the constant eddy viscosity formulation and figure (b) shows the result for the k-ε turbulence formulation. In the figure, the contour plots of the basic flow u_b as a function of the scaled vertical coordinate z and the scaled time (in units of the tidal period) is shown. The result for the constant eddy viscosity formulation reveals lower flow velocities near the bed compared to the k-ε turbulence formulation. Furthermore, the figure shows a higher maximum velocity of the flow for the constant eddy viscosity formulation. For both models the maximum positive basic flow is stronger than their negative flow values, revealing asymmetry in the basic flow.

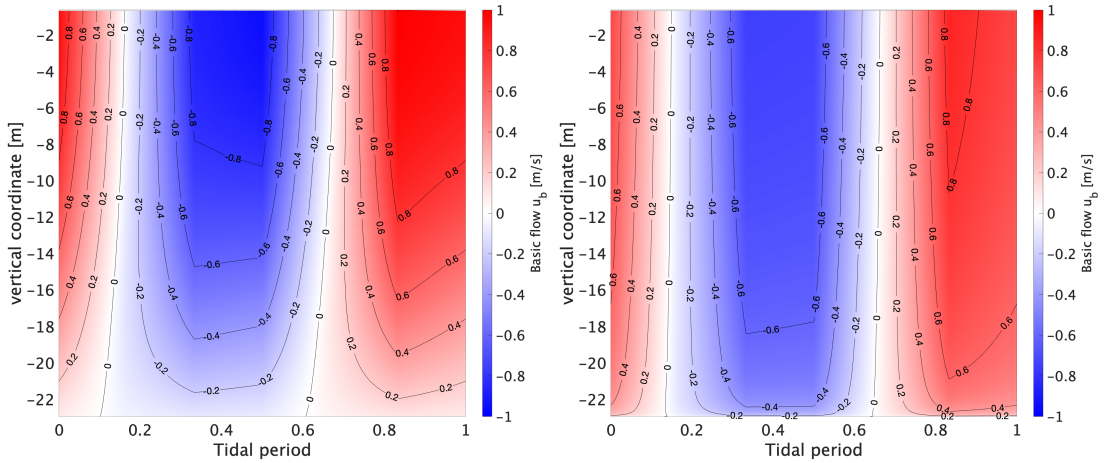

(a) Constant eddy viscosity formulation

(b) k-ε turbulence formulation

Figure 5.15: Contour plot of the basic flow u_b as a function of the scaled vertical coordinate z and of the scaled time (in units of the tidal period) for (a) Constant eddy viscosity formulation and (b) the k-ε turbulence formulation. Vertical coordinate is shown on the vertical axis, horizontal axis shows the time in units of the tidal period.

5.2.2 Results of the nominal case

The growth rate and migration as function of the topographic wave number k is investigated for both turbulence formulations, the results are shown in figure 5.16. Here, the wave number is varied in a range from $k = 4.9 \cdot 10^{-2}$ m^{-1} to $k = 5.0 \cdot 10^{-3}$ m^{-1}. Figure 5.16 (a) shows the growth rates per year, where the constant eddy viscosity formulation is depicted with a solid line, the k-ε turbulence formulation with a dotted line. It can be seen that no sand waves will form for the constant eddy viscosity formulation. For the k-ε turbulence formulation there is generation of sand waves. The most unstable computed sand wave is located at $k = 3.0 \cdot 10^{-2}$ m^{-1} corresponding to a wave length of $\lambda = 209$ m. The fast growing mode reaches a growth rate of $\Gamma_r = 1.18 \cdot 10^{-1}$ yr^{-1}. Figure 5.16 (b) shows the migration rate. Since there is no transport of sediment in the constant eddy viscosity formulation, there is no migration. The migration rate corresponding to the fast growing mode for the k-ε turbulence formulation is $c_m = 3.4$ m yr^{-1}.

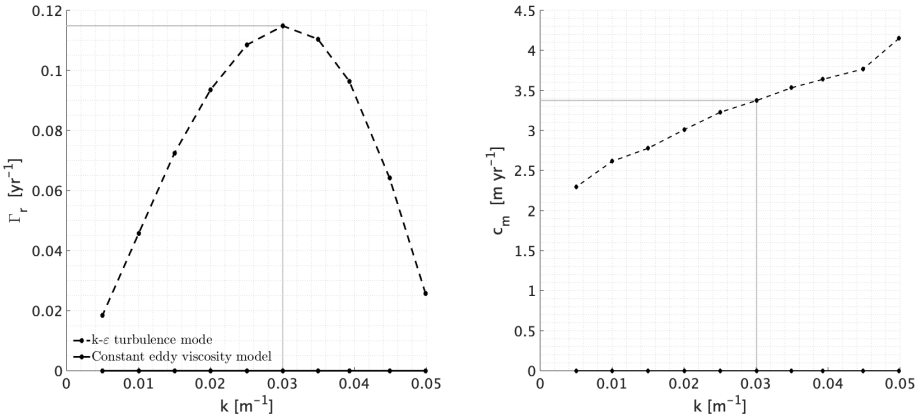

Figure 5.16: (a) Growth rates Γ_r [yr^{-1}] and (b) migration rate c_m [m yr^{-1}] for the constant eddy viscosity formulation (solid line) and the k-ε turbulence formulation (dotted line). The selection of the fast growing mode and the corresponding growth- and migration rates are indicated by the gray line.

Residual circulation

The residual recirculating cells are shown for both eddy viscosity formulations in Figure 5.17, where (a) shows the residual cells for the constant eddy viscosity formulation and (b) for the k-ε turbulence formulations. Here, the applied bed undulations follow from the result of the nominal case and are chosen to have a wavelength of $\lambda = 209$ m for both turbulence formulations. It can be seen that in the lower part of the cells, the flow is directed towards the crests. For the constant eddy viscosity formulation the circulation cells are concentrated at a larger vertical domain compared to the k-ε turbulence formulation. This results in a lowered center of the residual cells, from -21.8 m for the constant eddy viscosity formulations to -22.5 m for the k-ε turbulence formulations.

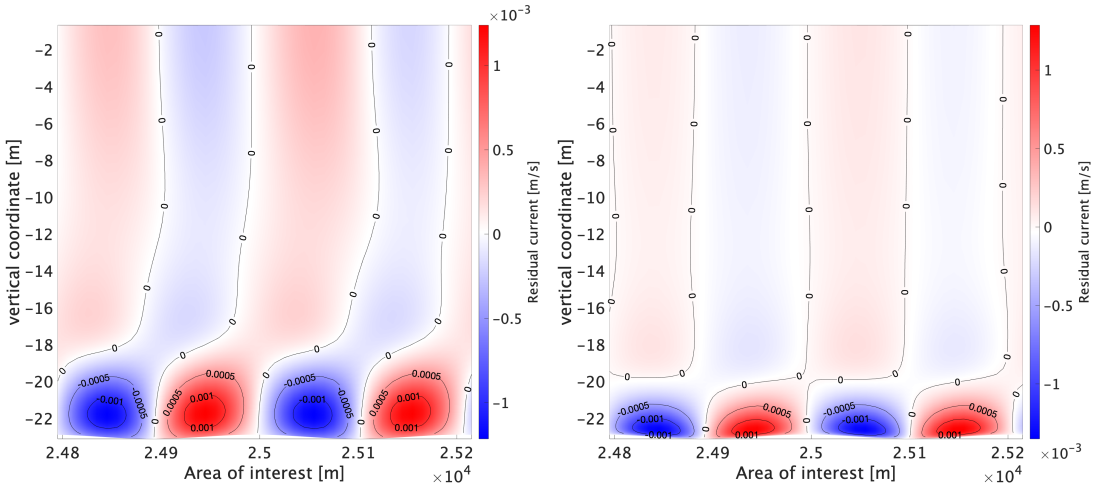

(a) Constant eddy viscosity formulations

(b) k-ε turbulence formulations

Figure 5.17: The residual current for the (a) constant eddy viscosity formulations and (b) the k-ε turbulence formulations. Vertical coordinate is shown on the vertical axis, horizontal axis shows the area of interest, which is the center of the model domain.

5.3 Summary of the results for the nominal case

Table 5 shows a summary of the results for the nominal case. Here an overview is given of the obtained results with the linear stability model and the numerical model along with the observed values for sand wavelengths and sand wave migration at the HKZ. It can be seen that the results obtained with the newly formulated closure relations agree more with the observations than the closure relations of HB01.

Table 5: Overview of modelled results obtained with the linear stability model and the numerical model for the nominal case. Also in the table are the observed values for sand wavelengths and sand wave migration at the HKZ.

Nominal case: Linear stability model	
	Value
New formulation of the closure relation	
Preferred wavelength λ	435 m
Preferred migration c_m	1.61 m yr^{-1}
e-folding time	22.5 yr
Closure relation of Hulscher and van den Brink (2001)	
Preferred wavelength λ	690 m
Preferred migration c_m	1.29 m yr^{-1}
e-folding time	46 yr
Nominal case: Numerical model	
Constant eddy viscosity formulation	
Preferred wavelength λ	-
Preferred migration c_m	-
k-ε turbulence formulation	
Preferred wavelength λ	209 m
Preferred migration c_m	3.4 m yr^{-1}
Observed sand waves at the HKZ	
Mean wavelength	370 ± 116 m
Average migration	2.31 ± 1.15 m yr^{-1}

6 Discussion

6.1 Linear stability model

This study builds on earlier work of Besio et al. (2003, 2004) and references therein. The findings of this study give further support to the hypothesis that offshore tidal sand waves arise as inherent instabilities of the flat bottom subjected to tidal currents. The key mechanism, which leads to the growth of sand waves that is discussed by Hulscher (1996): the interaction between tidal currents and undulations on the bottom give rise to steady recirculating cells. When the streaming of the recirculating cells is directed from the through towards the crest and is strong enough to overcome the effect of gravity, which tend to move the sediment down slope towards the through, the undulations grow and give rise to preferred bottom patterns. Besio et al. (2003) uses the closure relation described by Hulscher and van den Brink (2001), where the values for the eddy viscosity A and stress s follow from environmental parameters. Furthermore, in the work of Besio, the sediment transport is calculated with the formulation of Meyer-Peter and Müller (1948) which accounts for the total bottom shear-stress. In order to compensate for the use of the total bottom shear-stress instead of skin friction in the sediment transport formula, Besio et al. (2003) uses a very small grain size. The work of van Santen et al. (2011) studied the closure relations used by Hulscher and van den Brink (2001) by introducing a tuning parameter. In the work of van Santen et al. (2011) the modeled sand waves agreeing well with observations when the stress parameter is multiplied by a factor 3.5.
In this thesis, results provide a more accurate description of the turbulence closure relations. This newly defined formulation of the closure relations leads to an increased stress. This increased stress gives rise to sand wavelengths that agree more with observations (see Table 5). Furthermore, the model allows for the possibility of sand transport stemming from skin friction only. Figure 5.5 shows that the growth rates are significantly reduced and that the preferred wavelength is much larger than observed. It turns out that the computed sand waves agree more with observations when the sediment transport formulation allows for the total bed shear-stress. It should be pointed out that the model does not account for suspended load effects. The effect of suspended load provides a relevant contribution to the time development of the bottom, as shown by Besio et al. (2006).
The results of the sensitivity to sand wave characteristics on the water depth is expected, where shallower waters lead to shorter sand wavelength. Due to the shallow waters the stress at the bottom is increase, which leads to shorter sand wavelengths. A similar response of sand wavelength on water depth is shown by van Santen et al. (2011). In the same study, the dependence of sand wavelength on grain size is investigated. Here van Santen et al. (2011) shows almost no dependence of the grain size on sand wavelength. However, Besio et al. (2003) uses a too small grain size in order to increase the stress, leading to shorter sand wavelength. The same behaviour of the sand wavelength is computed here, where the sand wavelength will decrease due to on a decrease in grain size.

6.1.1 The nominal case

In order to explain the difference of the sand wave characteristics on the closure relation, the individual terms that contribute to growth and migration are investigated. These terms follow from the temporal development of the bottom perturbation (equation 3.40) and are

$$\frac{d\Pi}{dT} = \Gamma\Pi\,, \quad \Gamma = -\langle 2\delta i Q\rangle\,, \tag{6.1}$$

$$Q = 12\left[\left|\frac{\delta\Psi_d}{\mu r}\frac{\partial u_b}{\partial z}\right|_{z=0} - \theta_c\right]^{1/2}\left[\frac{\delta\Psi_d}{\mu r}\left(\frac{\partial^2\Psi}{\partial z^2} + \delta^2\Psi + \frac{1}{2}\frac{\partial^2 u_b}{\partial z^2}\right)_{z=0} - \frac{i\gamma\delta}{2}\right]. \tag{6.2}$$

The following contributions of the temporal development of the bottom perturbation are investigated:

$$\Gamma_1 = \langle Q_b \cdot i\frac{\delta^2\Psi_d}{\mu r}\frac{\partial^2\Psi}{\partial z^2}\rangle\,,$$
$$\Gamma_2 = \langle Q_b \cdot i\frac{\delta^2\Psi_d}{\mu r}\delta^2\Psi\rangle\,,$$
$$\Gamma_3 = \langle Q_b \cdot i\frac{\delta^2\Psi_d}{\mu r}\frac{1}{2}\frac{d^2u_b}{dz^2}\rangle\,,$$
$$\Gamma_4 = \langle Q_b \cdot \frac{\gamma\delta^2}{2}\rangle\,,$$

where,

$$Q_b = \left\langle 24\left[\left|\frac{\delta\Psi_d}{\mu r}\frac{\partial u_b}{\partial z}\right|_{z=0} - \theta_c\right]\right\rangle. \tag{6.3}$$

Notice that the imaginary parts of Γ_n contributes to the migrating character of the sand wave, whilst the real parts of Γ_n contribute to growth characteristics of initial sand wave formation.

Contribution to temporal development of the bottom perturbation due to Γ_1

Figure 6.1 shows that the term Γ_1 contributes for both the growth and migration rates for two turbulence closure relations. Here, the solid line indicates the model run preformed with the newly defined closure relations and the dotted line follows from the model run with the closure relations described by HB01.

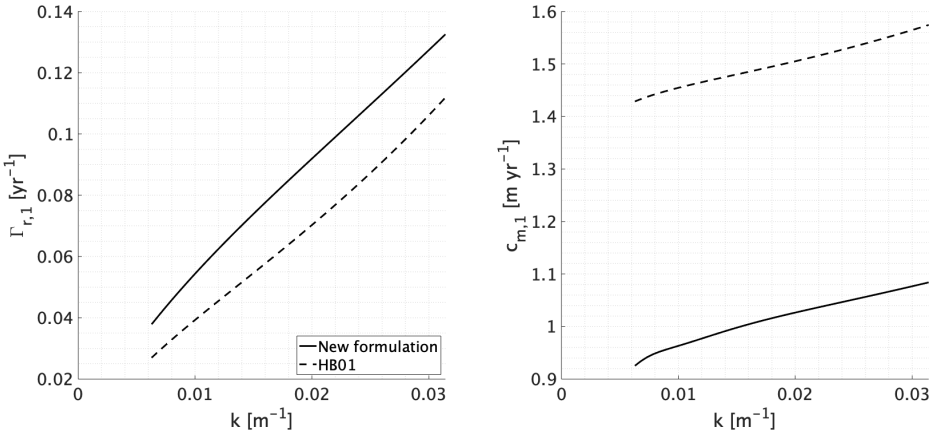

Figure 6.1: Left, the contribution to the growth and right, the contribution to the migration as function of the wave number. Due to the term Γ_1. The solid line is the model run done with the newly defined closure relations, the dotted line of HB01.

Contribution to temporal development of the bottom perturbation due to Γ_2

Figure 6.2 shows the model results of term Γ_2 for both closure relations. It can be seen that the model computes only contributes to migration rate for both closure relations. The migration speed for the newly defined closure relation is less compared to the relation of HB01. Furthermore, it can be seen that the model does not compute any growth rates for the term Γ_2. This is not expected from equations (6.1) and (6.2), indicating that further investigation into this term is needed.

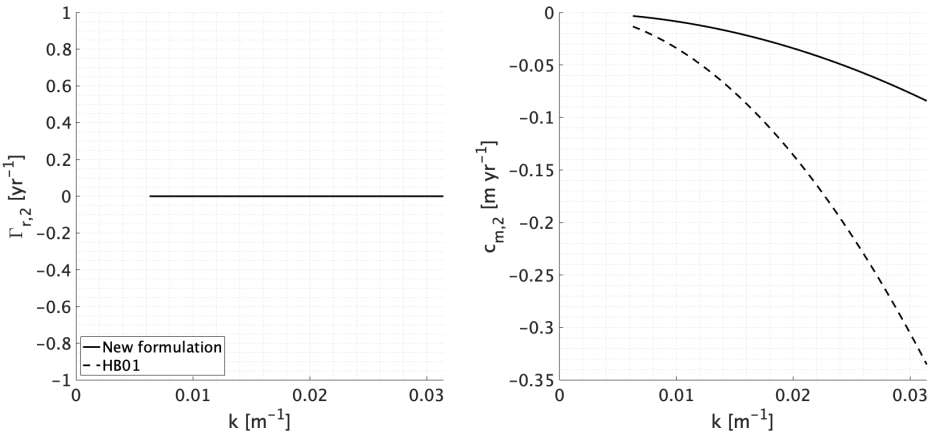

Figure 6.2: Left, the contribution to the growth and right, the contribution to the migration as function of the wave number. Due to the term Γ_2. The solid line is the model run with the newly defined closure relations, the dotted line of HB01.

Contribution to temporal development of the bottom perturbation due to Γ_3

Figure 6.3 shows the model results of term Γ_3 for both closure relations. It can be seen that the term Γ_3 only contributes to the migration of sand waves. This is expected since the term only consist of an imaginary part. However, the behaviour of the closure relations are rather different. For the newly formulated closure relations the term adds positive migration rates, unlike the response on the closure relation described by HB01 where the term leads to negative migration. It can also be seen that both responses are unrelated to the bottom perturbations and that the magnitude of the term for the new formulation is larger. In order to identify the origin that causes the 'flip' of the response in the 3rd term, further investigation of the term Γ_3 is needed.

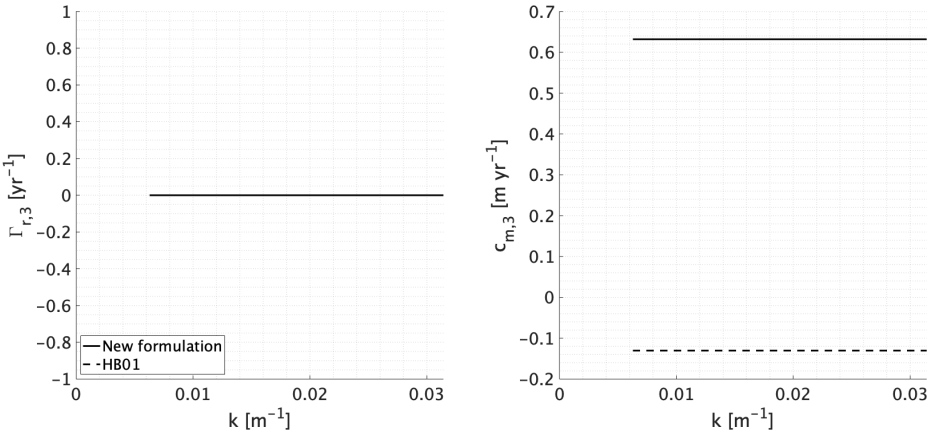

Figure 6.3: Left, the contribution to the growth and right, the contribution to the migration as function of the wave number. Due to the term Γ_3. The solid line is the model run done with the newly defined closure relations, the dotted line of HB01.

In order to explain the 'flip' observed in figure 6.3 a closer look into the isolated effects tidal current amplitude ratio is needed. Figure 6.4 shows the contribution due to Γ_3 for model runs where only the

tidal current amplitude ratios of M0/M2 or M4/M2 is accounted for. This is required to investigate the contributions of the considered tidal amplitude ratios, since the analytical expression reveals different values for the residual M0 (see equation 3.16) for both closure relations. Figure 6.4 shows the newly formulated closure relation in the left panel, the closure relation described by HB01 is shown on the right. It can be seen that for both relations the contribution of M4/M2 leads to positive migration rates whilst the M0/M2 amplitude ration contributes to negative migration rates. Furthermore, the amplitude ratio of M4/M2 is stronger than the M0/M2 for the newly described closure relations. The opposite is true for the closure relation of HB01. The behaviour shown in figure 6.4 explains the sign flip for both closure relations in figure 6.3.

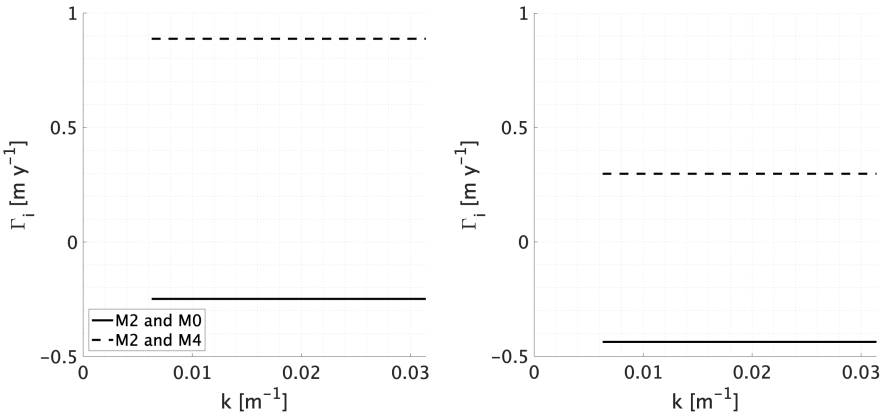

Figure 6.4: The contribution of Γ_3 for model runs where only the tidal current amplitude ratios of M0/M2 or M4/M2 is accounted for. Left follows from the newly defined closure relations, right follows from the model run with the closure relations described by HB01.

6.2 Numerical model

The result of figure 5.16 show that there is no movement of sediment for the model runs with a constant eddy viscosity model. In the Delft3D-FLOW model it is only possible to gain control over the eddy viscosity, the stress at the bottom is computed by the numerical model itself. In figure 5.15 it can be seen that the basic flow at the bottom for the constant eddy viscosity model attains a lower value compared to the k-ε turbulence model. The lowered value of the basic flow indicates a lower stress at the bottom. The stress can be computed form the characteristic velocity magnitude u_{char} located at height of z_{char} above the bed. The expression follows

$$\tilde{s} = \frac{8}{3\pi} \frac{u_{\text{char}}}{\ln\left(1 + z_{\text{char}}/z_0\right)} \,. \tag{6.4}$$

In figure 6.5 the stress value is plotted for two tidal cycles. This is done for the location in the centre of the domain. It can be seen that the stress reaches a value of $\tilde{s} = 0.028$ m^{-1} when the model deploys the constant eddy viscosity model. This is significantly smaller than the stress computed with the linear stability model.

However, the results of a study by Borsje et al. (2013) show do show sand wave formation for a constant eddy viscosity model. In this work the initial set-up is similar to this thesis. The main difference is the formulation of the sediment transport formula. Borsje et al. (2013) uses the sediment transport formulation described by Van Rijn (1993). This indicates that further investigation is needed into the formulation of the sediment transport formula employed by the numerical model.

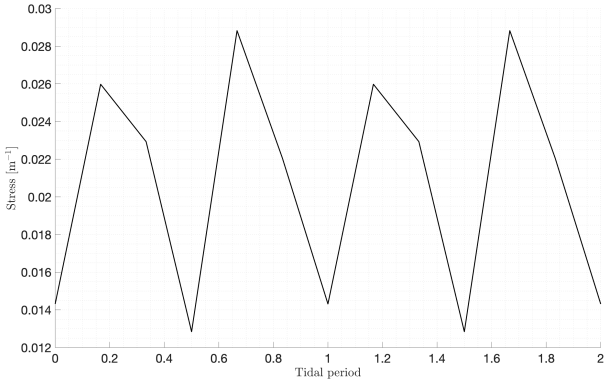

Figure 6.5: Stress value for two tidal cycles from the numerical model run with the constant eddy viscosity model. For an eddy viscosity of $A = 0.0185$ m^{2}s^{-1} the stress reaches a value of $\tilde{s} = 0.028$ m^{-1}

6.3 Limitations

In this research only the tidal forcing is taken into account. However, the effects of other physical processes is not taken into account. Observational studies show that wind, wave processes can significantly affect the evolution of the finite height of sand wave (Terwindt, 1971), which is shown with a model study Campmans et al. (2017).

Sand waves are predominantly rhythmic features in one spatial direction with their crests orthogonal to the direction of the tidal flow (Hulscher, 1996). However, along crest variations do exist, meaning that sand waves are a three dimensional phenomenon. In order to capture the influence of along crest variations of sand waves a 3D approach has to be employed. Blondeaux and Vittori (2009) carried out a weakly nonlinear analysis for which they find that 3D topographies similar to observed sand wave.

Finally, being based on a linear approach, the model can predict only the initial stage of sand wave formation. In order to investigate the finite-height a nonlinear approach is required.

7 Conclusion

The initial formation of offshore tidally generated sand waves was successfully reproduce in a linear stability model. This further support to the hypothesis that offshore tidal sand waves arise as inherent instabilities of the flat bottom subjected to tidal currents. Where the key mechanism is the interaction between tidal currents and undulations on the bottom give rise to steady recirculating cells. When the streaming of the recirculating cells is directed from the through towards the crest undulations grow and give rise to bottom patterns.

The model was run with two closure relations: a newly formulated closure relation and the closure relation defined by Hulscher and van den Brink (2001). Employing the new formulation of the closure relations, increases the bottom stress and enhances the growth of sand waves. The model utilizing both closure relations was was used to compute sand wave characteristics for a specific environment in the southern North Sea. The computed sand waves for the newly formulated closure relation result in a sand wavelength of 435 m and a migration speed of 1.61 m yr^{-1}. For the closure relations defined by Hulscher and van den Brink (2001), the model computes sand wavelength of 690 m and a migration speed of 1.29 m yr^{-1}.

Next, the results are compared to field data on sand wave length of the southern North Sea. For the site considered, the newly formulated closure relation showed good agreement of the observed sand wave data, where the closure relations defined by Hulscher and van den Brink (2001) overestimates the wave length of the sand waves.

The model does not allow for the suspended load effect and incorporates the total bottom shear-stress in the sediment transport formulation. The influence of form drag, which is part of the total bottom shear-stress, into the sediment transport formulation is investigated. The model shows that by exclusion of form drag the sand wave length is overestimated and attain very small growth rates $O(10^{-3}\ yr^{-1})$. So, next to skin friction the inclusion of form drag into the sediment transport formulation is needed to model realistic sand wavelength.

Furthermore, an exploration of the sand wave characteristics to environmental parameters is presented. The sensitivity to sand wave characteristics on the water depth, grain size, tidal amplitude ratios and their relative phase difference are investigated. The results reveal a strong dependence of the sand wavelength to the water depth, where deeper waters lead to longer sand wavelength. However, deeper waters will lower the migration speed of the sand waves. The sand wavelength will increase due to on a increasing grain size. The grain size does not effect the migration speed of sand waves strongly. Migration of sand waves opposite to the direction of the residual current are computed, due to the relative phase differences between the M4 and the M2. The dependence of sand waves characteristics to the residual current is only noticeable in the migration speed. The residual current has no effect on the sand wavelength.

Next, the sand wave characteristics for a specific environment were modeled in a numerical shallow water model (Delft-3D). The model was run with two turbulence models: constant vertical eddy viscosity and an advanced spatially and temporally variable vertical eddy viscosity model (k–ε turbulence model). Here the value for the eddy viscosity followed from the newly defined turbulence model. For the same tidal conditions, the constant vertical eddy viscosity model showed no initial formation of sand wave. The k–ε turbulence model computed sand wavelengths of 209 m and a migration speed of 3.4 m yr^{-1}.

References

Aliotta, S. and Perolli, G. M. E. (1987). A Sand Wave Field in the Entrance To Bahia Blanca. *Marine Geology*, 76:1–14.

Besio, G., Blondeaux, P., Brocchini, M., Hulscher, S. J. M. H., Idier, D., Knaapen, M. A. F., Németh, A. A., Roos, P. C., and Vittori, G. (2008). The morphodynamics of tidal sand waves: A model overview. *Coastal Engineering*, 55(7-8):657–670.

Besio, G., Blondeaux, P., Brocchini, M., and Vittori, G. (2004). On the modeling of sand wave migration. *Journal of Geophysical Research C: Oceans*, 109(4).

Besio, G., Blondeaux, P., and Frisina, P. (2003). A note on tidally generated sand waves. *Journal of Fluid Mechanics*, (485):171–190.

Besio, G., Blondeaux, P., and Vittori, G. (2006). On the formation of sand waves and sand banks. 557:1–27.

Blondeaux, P. (2001). Mechanics of coastal forms. *fluid mechanics*.

Blondeaux, P. and Vittori, G. (2009). Three-dimensional tidal sand waves. *Journal of Fluid Mechanics*, 618:1–11.

Boggs, S. (1974). Sand-Wave Fields in Taiwan Strait. *Geology*, 2(5):251–253.

Borsje, B. W., Roos, P. C., Kranenburg, W. M., and Hulscher, S. J. M. H. (2013). Modeling tidal sand wave formation in a numerical shallow water model: The role of turbulence formulation. *Continental Shelf Research*, 60:17–27.

Bouma, A. H., Rappeport, M. L., Orlando, R. C., and Hampton, M. A. (1980). Identification of bedforms in lower cook inlet, Alaska. *Sedimentary Geology*, 26(1-3):157–177.

Burchard, H., Craig, P. D., Gemmrich, J. R., van Haren, H., Mathieu, P. P., Meier, H. E., Smith, W. A. M., Prandke, H., Rippeth, T. P., Skyllingstad, E. D., Smyth, W. D., Welsh, D. J., and Wijesekera, H. W. (2008). Observational and numerical modeling methods for quantifying coastal ocean turbulence and mixing. *Progress in Oceanography*, 76(4):399–442.

Campmans, G. H. P. (2018). *Modeling storm effects on sand wave dynamics*.

Campmans, G. H. P., Roos, P. C., de Vriend, H. J., and Hulscher, S. J. M. H. (2017). Modeling the influence of storms on sand wave formation: A linear stability approach. *Continental Shelf Research*, 137(January):103–116.

Damen, J. M., van Dijk, T. A., and Hulscher, S. J. (2018). Spatially Varying Environmental Properties Controlling Observed Sand Wave Morphology. *Journal of Geophysical Research: Earth Surface*, 123(2):262–280.

Deigaard, R. and Fredsœ, J. . (1992). *Mechanics of coastal sediment transport*, volume 3. World scientific publishing company, Advanced series of Ocean Engineering.

Deltaris (2014). *Delft3D-FLOW user manual*. Deltaris, Delft.

Dodd, N., Blondeaux, P., Calvete, D., De Swart, H. E., Falqués, A., Hulscher, S. J., Rózyński, G., and Vittori, G. (2003). Understanding Coastal Morphodynamics Using Stability Methods. *Journal of Coastal Research*, 19(4):849–865.

Dorst, L. L., Roos, P. C., and Hulscher, S. J. (2011). Spatial differences in sand wave dynamics between the Amsterdam and the Rotterdam region in the Southern North Sea. *Continental Shelf Research*, 31(10):1096–1105.

Dorst, L. L., Roos, P. C., and Hulscher, S. J. (2013). Improving a bathymetric resurvey policy with observed sea floor dynamics. *Journal of Applied Geodesy*, 7(1):51–64.

Dronkers, J. (2005). *Dynamics Of Coastal Systems*. World Scientific Publishing Co Pte Ltd, Singapore.

Duffy, G. P. and Hughes-Clarke, J. E. (2005). Application of spatial cross correlation to detection of migration of submarine sand dunes. *Journal of Geophysical Research: Earth Surface*, 110(4):1–11.

Dyer, K. (1986). Coastal and estuarine sediment dynamics. John Wiley and Sons, Chichester, Sussex (UK), 358 edition.

Fredsøe, J. (1974). On the development of dunes in erodible channels. *Journal of Fluid Mechanics*, 64(1):1–16.

Gao, P. (2010). A general bedload transport equation for homogeneous grains.

Gerkema, T. (2000). A linear stability analysis of tidally generated sand waves. *Journal of Fluid Mechanics*, 417:303–322.

Gerkema, T. (2019). Tides in Coastal Seas and Basins. *An Introduction to Tides*, 122:122–156.

Hommes, S., Hulscher, S. J., and Stolk, A. (2007). Parallel modeling approach to assess morphological impacts of offshore sand extraction. *Journal of Coastal Research*, 23(6):1565–1579.

Hulscher (1996). Tidal-induced large-scale regular bed form patterns in. 101(96):51–54.

Hulscher, S. J., de Swart, H. E., and de Vriend, H. J. (1993). The generation of offshore tidal sand banks and sand waves. *Continental Shelf Research*, 13(11):1183–1204.

Hulscher, S. J. and van den Brink, G. M. (2001). Comparison between predicted and observed sand waves and sand banks in the North Sea. *Journal of Geophysical Research: Oceans*, 106(C5):9327–9338.

Huthnance, J. M. (1982). On the formation of sand banks of finite extent. *Estuarine, Coastal and Shelf Science*, 15(3):277–299.

Ikehara, K. and Kinoshita, Y. (1994). Distribution and origin of subaqueous dunes on the shelf of Japan. *Marine Geology*, 120(1-2):75–87.

Knaapen, M. A. (2005). Sandwave migration predictor based on shape information. *Journal of Geophysical Research: Earth Surface*, 110(4):1–9.

Knaapen, M. A. F. and Hulscher, S. J. M. H. (2002). Regeneration of sand waves after dredging. 46:277–289.

Krabbendam, J. (2018). *Modelling the long term evolution of observed tidal sand waves in the North Sea*. PhD thesis, Utrecht University.

Lesser, G. R., Roelvink, J. A., van Kester, J. A., and Stelling, G. S. (2004). Development and validation of a three-dimensional morphological model. *Coastal Engineering*, 51(8-9):883–915.

McCave, I. (1971). Sand waves in the North Sea off the coast of Holland. 1971:59–76.

Meyer-Peter, E. and Müller, R. (1948). Formulas for Bed-Load Transport. *Proceedings of the 2nd Meeting of the International Association of Hydraulic Research*, pages 39–64.

Németh, A. A., Hulscher, S. J., and Van Damme, R. M. (2007). Modelling offshore sand wave evolution. *Continental Shelf Research*, 27(5):713–728.

Németh, A. A., Hulscher, S. J. M. H., and De Vriend, H. J. (2002). Modelling sand wave migration in shallow shelf seas. *Continental Shelf Research*, 22(18-19):2795–2806.

Nikuradse, J. (1933). No Title. *NACA Technical, Memorandum 1292*.

Passchier, S. and Kleinhans, M. G. (2005). Observations of sand waves, megaripples, and hummocks in the Dutch coastal area and their relation to currents and combined flow conditions. *Journal of Geophysical Research: Earth Surface*, 110(4):1–15.

Pawlowicz, R., Beardsley, B., and Lentz, S. (2002). Classical tidal harmonic analysis including error estimates in MATLAB using TDE. *Computers and Geosciences*, 28(8):929–937.

Perillo, G. M. and Ludwick, J. C. (1984). Geomorphology of a sand wave in lower Chesapeake Bay, Virginia, U.S.A. *Geo-Marine Letters*, 4(2):105–112.

Rijksoverheid (2021). Windenergie op zee.

Shields, A. (1936). *Anwendung der Ahnlichkeitsmechanik und der Turbulenzforschung auf die Geschiebebewegung*. PhD thesis, Technical University Berlin.

Sleath, J. (1984). *Sea Bed Mechanics*.

Soulsby, R. (1998). Dynamics of Marine Sands (HR Wallingford Titles): A Manual for Practical Applications.

Swift, D. J., Parker, G., Lanfredi, N. W., Perillo, G., and Figge, K. (1978). Shoreface-connected sand ridges on American and European shelves: A comparison. *Estuarine and Coastal Marine Science*, 7(3):257–273.

Terwindt, J. H. (1971). Sand waves in the southern bight of the North Sea. *Marine Geology*, 10(1):51–67.

Van Alphen, J. and Damoiseaux, M. (1989). A geomorphological map of the Dutch shoreface and adjacent part of the continental shelf. *Geologie Mijnbouw*, 68:433–444.

van den Berg, J., Sterlini, F., Hulscher, S. J., and van Damme, R. (2012). Non-linear process based modelling of offshore sand waves. *Continental Shelf Research*, 37:26–35.

van Gerwen, W., Borsje, B. W., Damveld, J. H., and Hulscher, S. J. M. H. (2018). Modelling the effect of suspended load transport and tidal asymmetry on the equilibrium tidal sand wave height. *Coastal Engineering*, 136(January):56–64.

Van Rijn, L. C. (1991). Sediment transport in combined currents and waves.

Van Rijn, L. C. (1993). *Principles of sediment transport in rivers, estuaries and coastal seas*.

van Santen, R. B., de Swart, H. E., and van Dijk, T. A. G. P. (2011). Sensitivity of tidal sand wavelength to environmental parameters: A combined data analysis and modelling approach. *Continental Shelf Research*, 31(9):966–978.

van Veen, J. (1935). Sand waves in the North Sea. *Hydrographical Review*, 12(pp):21–29.

Vittori, G. (1989). Mouvement oscillatoire non-linéaire d'un fluide visqueux sur un fond présentant des ondulations de petite amplitude. *Journal of Hydraulic Research*, 27(2):267–280.

Vittori, G. and Blondeaux, P. (2020). River Dunes and Tidal Sand Waves: Are They Generated by the Same Physical Mechanism? *Water Resources Research*, 56(5):1–7.

Zhou, J. (20118). Modelling sand wave fields on the Taiwan banks, Northern South China sea: The formation of two-scale sand waves in different periods. *Netherlands centre for coastal research*, 39(3):307–491.

Zimmerman, J. T. F. (1981). Dynamics, diffusion and geomorphological significance of tidal residual eddies. *Nature*, 290(5807):549–555.

Appendices

A New formulation of the turbulence closure relations

Where Hulscher and van den Brink (2001) used a constant eddy viscosity profile $A = \text{cst}.$, leading to expression (3.8) for the eddy viscosity and stress parameter. A different approach on the distribution is presented here, which follows from personal communication with Prof. Huib de Swart. Where in this approach a thin layer near the bed of thickness δ_l is added in order to include the log layer near the bed where the vertical flow profile is assumed to be logarithmic. The velocity profile in this layer will be:

$$u = \frac{u_*}{k} \ln\left(\frac{\delta_l + z_0}{z_0}\right). \tag{A.1}$$

In the layer δ_l the eddy viscosity distribution is parabolic and defined by:

$$A = k|u_*|(z + z_0)(1 - \frac{z}{h}) \qquad 0 \le z \le \delta_l \tag{A.2}$$

where h is the total water level corrected for the thickness of the log layer δ_l. In the layer $0 \le z \le \delta_l$, the flow if logarithmic and is described by equation (2.8). The corresponding depth-average velocity reads:

$$\begin{aligned} \langle u \rangle &= \frac{1}{h + z_0} \int_0^h u \ \mathrm{d}z = \frac{u_*}{\kappa(h + z_0)} \left[(z + z_0) \ln\left(\frac{z + z_0}{z_0}\right) - z \right]_0^h \\ &= \frac{u_*}{\kappa} \left[\ln\left(\frac{h + z_0}{z_0}\right) - \frac{h}{h + z_0} \right] \end{aligned} \tag{A.3}$$

which leads to the following expression when $h \gg z_0$

$$\langle u \rangle = C u_*, \quad C = \frac{1}{\kappa} \left[\ln\left(\frac{h}{z_0}\right) - 1 \right], \tag{A.4}$$

where C is the conductance coefficient. Next, consider the following simplified momentum balance,

$$0 = -g \frac{\partial \eta}{\partial x} + \frac{\partial}{\partial z}\left(A \frac{\partial u}{\partial z}\right), \tag{A.5}$$

Along with the following boundary conditions:

$$A \frac{\partial u}{\partial z} = 0 \quad \text{at} \quad z = 0, \tag{A.6}$$

$$A \frac{\partial u}{\partial z} = |u_*| u_* \quad \text{at} \quad z = h. \tag{A.7}$$

It follows that the shear stress $A\partial u/\partial z$ depends linearly on z, for any given choice on A. The solution for the shear stress will be:

$$A \frac{\partial u}{\partial z} = |u_*| u_* \left(1 - \frac{z}{h}\right). \tag{A.8}$$

Substituting this back into the simplified momentum balance (A.5) and integrating over z gives

$$g h \frac{\partial \eta}{\partial x} = -|u_*| u_*. \tag{A.9}$$

It follows from the momentum balance (A.5) that for a constant A and substituting expression (A.9) it will read

$$0 = \frac{|u_*|u_*}{h} + A\frac{\partial^2 u}{\partial z^2}\,. \tag{A.10}$$

In the layer $\delta_l \le z \le h$ the eddy viscosity remains constant and is given by

$$A = k|u_*|(\delta_l + z_0)(1 - \frac{\delta_l}{h})\,. \tag{A.11}$$

So, in the layer where the eddy viscosity remains constant the momentum balance reads

$$\frac{\partial^2 u}{\partial z^2} = \frac{-|u_\star|u_\star}{Ah}\,. \tag{A.12}$$

Integrating this equation twice with respect to z gives the following solution for u

$$u = \frac{-|u_\star|u_\star}{Ah}\left[\frac{1}{2}z^2 + C_1 z\right] + C_2\,. \tag{A.13}$$

Here C_1, C_2 are integration constants which follow from the following boundary conditions

$$u = 0 \quad \text{at} \quad z = h\,, \tag{A.14}$$

$$\frac{\partial u}{\partial z} = su \quad \text{at} \quad z = \delta_l\,. \tag{A.15}$$

Here, the stress parameter s is introduced by defining the partial slip condition at the top of the boundary layer $z = \delta_l$. It is assumed the velocity u is continuous at $z = \delta_l$ and has a logarithmic flow profile (Eq. 2.8):

$$u = \frac{u_*}{k}\ln\left(\frac{\delta_l + z_0}{z_0}\right) \tag{A.16}$$

Applying boundary conditions (A.14) and (A.15) yield the following integration constants

$$C_1 = -h\,, \tag{A.17}$$

$$C_2 = \frac{u_*}{k}\ln\left(\frac{\delta_l + z_0}{z_0}\right) - \frac{-|u_\star|u_\star}{Ah}\delta_l\big(h - \frac{1}{2}\delta_l\big)\,. \tag{A.18}$$

The expression for the stress parameter s is given by:

$$s = \frac{\frac{-|u_\star|u_\star}{Ah}\frac{h-\delta_l}{h}}{\frac{u_*}{k}\ln\left(\frac{\delta_l+z_0}{z_0}\right)} = \frac{|u_*|k}{A}\frac{(h-\delta_l)}{h\ln\left(\frac{\delta_l+z_0}{z_0}\right)}\,. \tag{A.19}$$

Plugging in the expression for A (A.2) gives

$$s = \frac{1}{\delta_l + z_0}\frac{1}{\ln\left(\frac{\delta_l+z_0}{z_0}\right)} \tag{A.20}$$

The expressions for s and A still depend on the unknown δ_l. The value of this log-layer, δ_l, follows from the condition that the depth average velocity is independent of the value for A. The depth average velocity for a logarithmic flow profile and a parabolic eddy viscosity profile is already known (A.3),

$$\langle u\rangle = \frac{u_*}{k}\left[\ln\big(\frac{h+z_0}{z_0}\big) - \frac{h}{h+z_0}\right]. \tag{A.21}$$

For the new viscosity profile, the depth-average velocity reads:

$$\begin{aligned}\langle u \rangle =& \frac{1}{h+z_0}\int_0^{\delta_l} \frac{u_*}{k}\ln\left(\frac{z+z_0}{z_0}\right)dz \\ &- \frac{1}{h+z_0}\int_{\delta_l}^{h} \frac{|u_*|u_*}{Ah}\left[\frac{1}{2}(z^2-\delta_l^2) - h(z-\delta_l) - h(z-\delta_l)\right]dz \\ &+ \frac{u_*}{k}\ln\left(\frac{\delta_l+z_0}{z_0}\right)\frac{h-\delta_l}{h+z_0},\end{aligned} \tag{A.22}$$

or:

$$\begin{aligned}\langle u \rangle =& \frac{u_*}{k}\left[\frac{(\delta_l+z_0)\ln\left(\frac{\delta_l+z_0}{z_0}\right)}{h}\right] + \frac{u_*}{k}\frac{(h-\delta_l)}{h}\ln\left(\frac{\delta_l+z_0}{z_0}\right) \\ &+ \frac{u_*}{k}\left[\frac{\frac{1}{6}h^3 - \delta_l h^2 + \delta_l^2 h - \frac{1}{6}\delta_l^3}{h^2(\delta_l+z_0)(1-\frac{\delta_l}{h})}\right].\end{aligned} \tag{A.23}$$

Setting this equal to the result for the depth average velocity for a logarithmic flow profile and a parabolic eddy viscosity profile (A.3), which after development yields an expression for the depth δ_l:

$$(1+\hat{z_0})\ln\left(\frac{\hat{\delta_l}+\hat{z_0}}{\hat{z_0}}\right) - \hat{\delta_l} + \frac{\frac{1}{6} - \hat{\delta_l} + \hat{\delta_l}^2 - \frac{1}{6}\hat{\delta_l}^3}{(\hat{\delta_l}+\hat{z_0})(1-\hat{\delta_l})} = \ln\left(\frac{1}{\hat{z_0}}\right) - 1 \tag{A.24}$$

where $\hat{\delta_l} = \delta_l/h$ and $\hat{z_0} = z_0/h$. It turns out that for parameter settings of HKZ that $\delta_l \approx 1.44\,\text{m}$. Now the value for δ_l is known it can be plugged into expressions (A.11) and (A.20) for the eddy viscosity and the stress parameter respectively.

B The basic state

As the basic state a unidirectional tidal flow is taken over a flat bottom, the flow ($u = u_b(t, z)$, $w = 0$) is assumed to be driven by an oscillatory horizontal pressure gradient p of angular frequency σ

$$\frac{\partial p}{\partial x} = -P_{0x} - \sum_{n=1}^{2} \frac{P_{nx}}{2}(e^{in\sigma t} + c.c.)\,. \tag{B.1}$$

Here P_{1x} and P_{2x} are complex amplitudes of the oscillatory pressure gradient of the semi-diurnal (M2) and quarter-diurnal (M4) tidal wave constituents, respectively, and P_{0x} is a constant. The horizontal momentum equation reduce to

$$\frac{\partial u_b}{\partial t} = -\frac{1}{\rho}\frac{\partial p}{\partial x} + A_v \frac{\partial^2 u_b}{\partial z^2}\,, \tag{B.2}$$

with the boundary conditions

$$\frac{\partial u_b}{\partial z} = \tilde{s} u_b \quad \text{at} \quad z = 0\,, \quad \frac{\partial u_b}{\partial z} = 0 \quad \text{at} \quad z = H\,. \tag{B.3}$$

Plugging in the expressions for u_b and p_x, solving the differential equation and applying the boundary conditions, results in the solution for the basic state.

Residual component

First, only the residual component of the flow is considered.

$$0 = \frac{P_{0x}}{\rho} + A_V \frac{\partial^2 u_0}{\partial z^2} \tag{B.4}$$

Integrating above expression will with respect to z gives

$$A_V \frac{\partial u_0}{\partial z} = -\frac{P_{0x}}{\rho} z + C_1 \tag{B.5}$$

Filling in the boundary condition at the surface $z = H$ (rigid lid), such that $\partial u/\partial z = 0$ reveals the following condition for C_1

$$C_1 = \frac{P_{0x}}{\rho} H \tag{B.6}$$

This results in the following equation, which is integrate with respect to z and rearranged

$$A_V \frac{\partial u_0}{\partial z} = \frac{P_{0x}}{\rho}(H - z) \tag{B.7}$$

$$u_0 = \frac{P_{0x}}{\rho A_V}\left(Hz - \frac{1}{2}z^2\right) + C_2 \tag{B.8}$$

Making use of the boundary conditions for the bottom $z = 0$ to obtain an expression for the integration constant C_2

$$\frac{P_{0x}}{\rho A_V}(H - z)\bigg|_{z=0} = \bar{s}\left(\frac{P_{0x}}{\rho A_V}\left(Hz - \frac{1}{2}z^2\right) + C_2\right)\bigg|_{z=0} \tag{B.9}$$

$$C_2 = \frac{P_{0x}}{\rho A_V \tilde{s}} H \tag{B.10}$$

So the final result for the residual component of the basic state is

$$u_0(z) = \frac{P_{0x}}{\rho A_V}\left(Hz - \frac{1}{2}z^2\right) + \frac{P_{0x}}{\rho A_V \tilde{s}}H = -\frac{P_{0x}}{\rho A_V}\left(\frac{z^2}{2} - Hz - \frac{H}{\tilde{s}}\right) \tag{B.11}$$

M2 and M4 tidal component

Now the same approach is applied to the other tidal components (M2 and M4)

$$\sum_{n=1}^{2} \mathrm{in}\,\sigma u_n(z)e^{in\sigma t} + c.c. = \sum_{n=1}^{2}\frac{P_{nx}}{2\rho}e^{in\sigma t} + c.c. + A_V\sum_{n=1}^{2}\frac{\partial^2 u_n}{\partial z^2}e^{in\sigma t} + c.c. \tag{B.12}$$

For convenience the summation signs are dropped

$$-A_V\frac{\partial^2 u_n}{\partial z^2} + in\sigma u_n(z) = \frac{P_{nx}}{2\rho} \tag{B.13}$$

This is a second order, linear, non-homogeneous differential equation which has a solution in the form of

$$u_n(z) = -\frac{iP_{nx}}{2\rho n\sigma} + C_3 e^{(i+1)\sqrt{\frac{n\sigma}{2A_V}}z} + C_4 e^{-(i+1)\sqrt{\frac{n\sigma}{2A_V}}z} \tag{B.14}$$

Once again, the integration constants C_3 andC_4 can be found by applying the boundary conditions. From the boundary condition at the surface it follows that

$$C_3 = C_4 e^{-2(i+1)}\sqrt{\frac{n\sigma}{2A_V}}H \tag{B.15}$$

Substituting this into equation (B.14) gives

$$u_n(z) = -\frac{iP_{nx}}{2\rho n\sigma} + C_4 e^{-2(i+1)\sqrt{\frac{n\sigma}{2A_V}}H} e^{(i+1)\sqrt{\frac{n\sigma}{2A_V}}z} + C_4 e^{-(i+1)\sqrt{\frac{n\sigma}{2A_V}}z} \tag{B.16}$$

$$= -\frac{iP_{nx}}{2\rho n\sigma} + C_4 e^{(i+1)\sqrt{\frac{n\sigma}{2A_V}}(z-2H)} + C_4 e^{-(i+1)\sqrt{\frac{n\sigma}{2A_V}}z} \tag{B.17}$$

In order to obtain the integration constant C_4, the boundary condition at the bed is applied, it turns out that

$$C_4 = -\frac{i\tilde{s}P_{nx}}{2\rho n\sigma}\left((i+1)\sqrt{\frac{n\sigma}{2A_V}}\left(e^{-2H(i+1)\sqrt{\frac{n\sigma}{2A_V}}} - 1\right) - \tilde{s}\left(e^{-2H(i+1)\sqrt{\frac{n\sigma}{2A_V}}} + 1\right)\right)^{-1} \tag{B.18}$$

The velocity in the basic state

Substituting everything into equation (B.2) gives the full expression for the velocity in the basic state

$$u_b(z,t) = -\frac{P_{0x}}{\rho A_V}\left(\frac{z^2}{2} - Hz - \frac{H}{\tilde{s}}\right) + \left[\sum_{n=1}^{2}\frac{P_{nx}}{2ni\rho\sigma}\left(1 + \tilde{c}_n\left(E_n^2 e^{-(i+1)\frac{z}{\Delta_n}} + e^{(1+i)\frac{z}{\Delta_n}}\right)\right)e^{in\sigma t} + c.c.\right] \tag{B.19}$$

Here, Δ_n is a viscous length defined in terms of the eddy viscosity A_v and of the angular frequency of the tidal oscillation σ,

$$\Delta_n = \sqrt{\frac{2A_v}{n\sigma}}\,, \quad E_n = e^{(1+i)\frac{H}{\Delta_n}}\,, \quad \tilde{c}_n = -\frac{\tilde{s}}{\tilde{s}(E_n^2+1) + (1+i)(E_n^2 - 1/\Delta_n)}\,. \tag{B.20}$$